ALMA MATER STUDIORUM · UNIVERSITY OF BOLOGNA

School of Science
Department of Physics and Astronomy
Master Degree in Physics

A new isotopic fragments identification with Lagrange Multipliers in the FOOT experiment

Supervisor:
Chiar.mo Prof. Mauro Villa

Co-supervisor:
Dr. Sofia Colombi

Submitted by:
Sara Maietti

Academic Year 2021/2022

Abstract

Hadrontherapy is one of the available techniques used nowadays to treat cancer. Specifically, it employs beams of protons or heavier ions with initial energies of hundreds of MeV/u. Hadrontherapy has an advantageous energy release in the patient, allowing to irradiate the cancer volume in a more precise way and to spare the healthy tissues surrounding it. The main drawback of this kind of therapy is the nuclear interaction of the primary beam with the nuclei constituting the irradiated tissue. Target and projectile nuclear fragmentation could have a dangerous biological effect on tissues surrounding the tumor. Specifically, target fragments have a very short range and are difficultly detected. For this reason the experimental panorama is very poor, thus reducing the precision in the evaluation of success or induced risk of hadrontherapy treatments. For this purpose, the FOOT (FragmentatiOn Of Target) experiment has been designed. It aims at filling the gap both in projectile and target fragmentation experimental data, measuring the fragment production cross section by using in the latter an inverse kinematic technique. At larger energies, the FOOT measurements will be useful to evaluate the interaction of the space radiation field with materials composing the spaceship hull in a long term space mission (typically on Mars), in order to assess the radiation-induced damage on astronauts' health and electronics on board. The FOOT apparatus allows to identify nuclear fragments by measuring their charge Z and their number of mass A. The latter is measured in three redundant ways, which need to be combined to obtain a best estimation of A. In the present thesis, the technique of Lagrange Multipliers used for the constrained minimization of functions, will be introduced and implemented in the FOOT analysis code to reconstruct the number of mass of nuclear fragments. Moreover, the results of the method will be compared to the ones already implemented in the experiment.

Contents

Introduction

Cancer is a disease caused by the uncontrollable growth of abnormal cells. Moreover, it has been listed by World Health Organization as the second leading cause of death globally in 2020 [1]. There are many techniques used to treat cancer, such as surgery, chemotherapy, immunotherapy and radiotherapy. The treatments aim at removing the cancer: when this is not possible, though, one can try to prevent the reproduction of its cells. In radiotherapy, beams of ionizing radiation are used to irradiate the tumor in order to damage the DNA of the cells. According to the type of radiation involved, one can have conventional radiotherapy or hadrontherapy. In the first case, X-Rays or electrons are used, while hadrontherapy uses beams of heavier charged particles, usually protons or ^{12}C ions. The reason for the choice of these particles stands in their interaction with matter, which produces the largest energy release at the end of their path in correspondence with the so-called *Bragg peak*. By modulating the initial energy and intensity of the beam, one can place the peak of energy release in correspondence of the tumor site, irradiating it in an uniform and effective way, sparing the healthy tissues and organs.

As opposed to the case of therapy with photons and electrons, which are well established techniques based on an accurate knowledge of radiation-matter interaction, charged particles have a side effect caused by nuclear fragmentation. In the energy range of charged particles therapy, i.e. between 60 and 400 MeV/u, fragmentation happens for the target in the case of protons and for target and projectile in the case of ^{12}C. The main drawback of target fragments is that they have very short range, thus they cannot exit the target and cannot be detected. This reflects in a lack of measurements for target fragmentation cross section. Due to this deficit of experimental data, the effect of the production of nuclear fragments in the human body is not completely understood and it is not yet included in the treatment planning system for hadrontherapy [2]. However, it is important to evaluate the contribution of fragments, mostly because of their biological effect in the healthy tissues. To deal with this problem and try to fill the vacancy in experimental measurements, the FOOT (FragmentatiOn Of Target) experiment has been conceived. FOOT aims at measuring the differential cross section, as a function of the energy and emission angle of fragments, for target fragmentation. To avoid the problem of the short range of target fragments, measurements are performed with an inverse kinematic approach. In this layout, a beam of C or O hits a composite target of C_2H_4 and C: the H cross section is obtained by subtraction. The experiment has been designed as a table-top apparatus and it consists of two setups: an emulsion spectrometer for the detection of light fragments with Z=1 and 2, and a magnetic spectrometer able to detect heavier fragments. Moreover, the setup of the experiment allows to obtain measurements for projectile fragmentation in a direct kinematic configuration. Hadrontherapy is not the only context in which the measurements of FOOT can be exploited: thanks to the overlap in particle type, energy range and physical processes occurring, space radioprotection can also benefit from the results of FOOT. As a matter of fact, fragmentation cross sections obtained with the magnetic spectrometer can be used for the estimation of dose received by astronauts and electronic equipment during long duration space missions.

The work of this thesis focuses on the electronic setup of FOOT. It is composed by a magnetic spectrometer, which allows to reconstruct the charge Z and mass number A of nuclear fragments: Z can be obtained from the energy loss of fragments in a thin scintillator and time of flight, while A is obtained in three different ways (A_1, A_2, A_3) using the momentum, time of flight and kinetic energy, thanks to the redundant measurements of the apparatus. The main goal of this thesis is to implement a technique able to combine the three mass number measurements A_1, A_2, A_3 using the Lagrange Multipliers method. This technique allows to obtain the best estimate of A (i.e., A_{fit}) that minimizes the Lagrangian function $\mathcal{L}$, which is usually built to perform the minimization of a function $f(x)$ that needs to satisfy some constraints $g_i(x)$.

In chapter 1, the basic radiation-matter interactions taking place during hadrontherapy are described, together with the introduction of some basic radiobiology quantities and the description of the common ground between radiation therapy and space radioprotection. A short historical review of hadrontherapy is also presented. Chapter 2 is dedicated to the FOOT experiment: the motivations and the two layouts of the apparatus are reported. In Chapter 3 the main work of this thesis is described, starting from the reconstruction of Z and A of fragments produced by a 200 MeV/u and a 700 MeV/u beam of ^{16}O on a C_2H_4 target. Then a theoretical description of the Lagrange Multipliers method is presented, together with an explanation of how it can be applied to the reconstruction of A_{fit} in the FOOT experiment.

The results of the number of mass A_{fit} reconstructed with the Lagrange Multipliers method, using simulated data of a 200 MeV/u beam of ^{16}O impinging in a target of C_2H_4, are shown and compared to the results of the other mass reconstruction techniques of FOOT, i.e. Augmented Lagrangian Method (ALM) and χ^2 minimization.

Chapter 1

Radiation-Matter Interaction

Radiotherapy is one of the many techniques used to treat solid tumors, particularly cancer. Its name comes from the tool used in this therapy to irradiate and treat tumors: ionizing radiation. By definition, a ionizing radiation is a particular kind of particle or electromagnetic wave that is able to release energy inside matter and ionize its atoms: the goal of radiotherapy is to ionize the DNA of tumor cells in order to destroy them or prevent their multiplication.

During treatment, it is important to take into account the fact that the irradiation of tumor cells is impossible to achieve without causing some effects also on the surrounding healthy tissues. Therefore, the purpose is to maximize the energy release on the tumor by monitoring two parameters. The former is the Tumor Control Probability (TCP), which is the probability that tumor cells can be controlled with the deposited radiation. The latter is Normal Tissue Control Probability (NTCP), which is the response of healthy tissues surrounding the tumor [3]. Both of them depend on biological effects, but generally they increase with dose, i.e. energy released per unit mass, as illustrated in Figure 1.1.

The two curves appear shifted along the x-axis because normal tissues can better repair radiation damage. The purpose of radiotherapy is thus to work in the range where TCP-NTCP is larger.

Nowadays, there are two different kinds of radiotherapy: conventional radiotherapy and hadrontherapy. The former uses beams of X-rays, while the latter exploits beams of charged particles, mainly protons and ^{12}C ions. The different kinds of radiation implied in these two treatments techniques can cause distinct physical interactions and biological effects in the irradiated tissue.

This chapter will contain, in section 1.1, the description of physical processes taking place in the interaction of charged particles with matter, both elec-

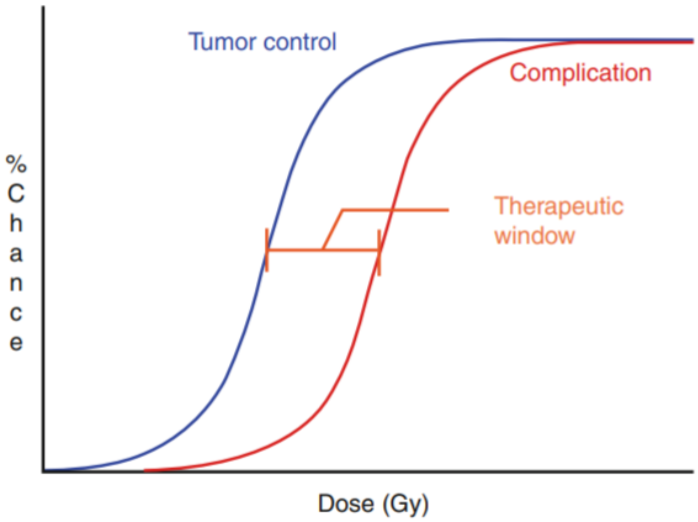

Figure 1.1: TCP (blue line) and NTCP (red line) probabilities as a function of energy released in the patient. Radiotherapy has to maximize the TCP-NTCP difference for a given dose and works in the therapeutic window [4].

tromagnetic and nuclear, in section 1.2 some parameters useful to describe the effect of ionizing radiation on living tissue are introduced. Section 1.3 presents a short overview of the beginning and development of hadrontherapy, and section 1.4 explains the common ground between hadrontherapy and space radioprotection.

1.1 Charged Particles Interactions with Matter

When a charged particle enters a slab of material, several kinds of interaction can happen. In the energy range of hadrontherapy, which is up to 250 MeV/u for proton beams and up to 400 MeV/u for ^{12}C ions, the interaction between a charged particle and an atom of the material can be either electromagnetic or nuclear. When an electromagnetic interaction happens, the particle can be subjected to an inelastic collision with electrons, causing ionization, or to an elastic collision with nuclei, causing multiple Coulomb scattering. Instead, nuclear interaction mainly produces fragmentation, which can involve both the projectile and the target, or just one of them, according to the size of the nuclei involved.

1.1.1 Electromagnetic Interaction

In the inelastic collision between a charged particle and an atomic electron, the particle can transfer energy to the electron and strip it from the nucleus, ionizing the atom.
Since for a single particle many collisions could happen, the quantity describing this process is the energy loss per unit length in a given medium, whose average is expressed by the Bethe-Bloch formula:

$$-\left\langle \frac{dE}{dx} \right\rangle = \frac{\rho \cdot Z}{A} \frac{4\pi N_A m_e c^2}{M_U} \left(\frac{e^2}{4\pi\epsilon_0 m_e c^2} \right)^2 \frac{z^2}{\beta^2} \left[ln\left(\frac{2m_e c^2 \beta^2}{I \cdot (1-\beta^2)} \right) - \beta^2 \right] \quad (1.1)$$

All the constants contained in equation (1.1) are explained in table 1.1.

ρ	Medium Density	Z	Medium Atomic Number
A	Medium Mass number	N_A	Avogadro Number: $6.022 \cdot 10^{23}$ mol^{-1}
m_e	Electron Mass: 0.510 MeV/c^2	M_U	Atomic Mass Unit
e	Electron Charge	ϵ_0	Vacuum Permittivity
z	Charge of the Incoming Particle	I	Mean Excitation Potential

Table 1.1: Constants of the Bethe Bloch formula

The most important dependencies in the formula are the charge z and the β parameter of the projectile particle: the higher the incoming particle charge, the larger its energy loss, while the $1/\beta^2$ term indicates that the particle loses less energy when it is faster, thus at the beginning of its path in the traversed medium. The energy release, then, increases as the particle slows down: the largest dE/dx happens at the end of the path of the particle, right before it stops. The general trend of the dE/dx function is illustrated in figure 1.2 for several particles.
The formula (1.1) can be applied with good precision only in the range $0.1 < \beta\gamma < 1000$. For all the other $\beta\gamma$ values some correction are needed:

- At low energies, the *shell correction* must be applied. In these conditions, the velocity of the incoming charged particle is comparable to the orbital velocity of atomic electrons and one of the assumptions of the Bethe-Bloch theory breaks down: the electron cannot be considered as stationary in the collision [5]. For this reason, at low velocities the effective charge of projectile particles decreases, due to the interplay of ionization and recombination and the term Z in equation (1.1) must be replaced with Z_{eff}:

$$Z_{eff} = Z\left[1 - exp\left(-125\beta Z^{-2/3}\right)\right] \quad (1.2)$$

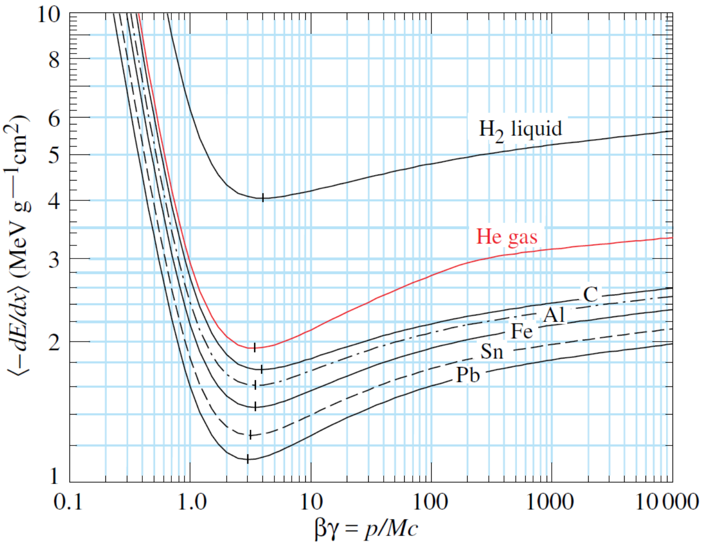

Figure 1.2: Mean Energy loss per unit length (quantity described in equation 1.1) as a function of $\beta\gamma$ of the incident charged particle.

At still lower projectile energies, another significant contribution arises: elastic collisions with target nuclei, which dominate the process at the end of the path of the particle. For radiotherapy applications, though, this contribution can be neglected [6].

- At high energies the *density correction* has to be taken into account. In this case, the effect produced by the beam of charged particles entering a medium is the polarization of atoms along its path, which results in a shielding of the farther electrons. These electrons will thus contribute less to the energy loss of the particle [5].

Considering the initial energy of the incoming beam, it is evident that hadrontherapy works in the top-left area of the plot in Figure 1.2 and has to take into account mainly the low energy correction, which is illustrated in figure 1.3 for ^{12}C ions and protons.
Considering plot 1.3, the goal of therapy is to choose a beam energy that allows to have the minimum stopping power in the entrance channel of the body and the peak of the stopping power in correspondence of the cancer volume: this can be done by tuning the initial energy of beam, which is reported on the x-axis of the same plot.
The Bethe Bloch formula (1.1) implicitly contains the main advantage of treating tumors with charged particles: due to the $1/\beta^2$ dependence of the

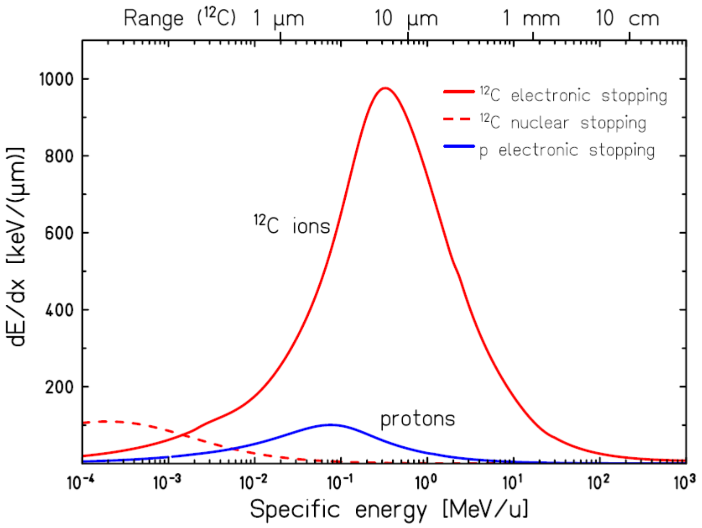

Figure 1.3: Stopping power of carbon ions (red line) and protons (blue line) as a function of the beam energy, in the low energy range [6].

average energy loss, the energy released as a function of the depth has a very characteristic shape, exhibiting a *Bragg peak* at the end of the path. Next section will contain a more detailed description of the Bragg peak and of its most efficient application in therapy.

Bragg Peak

Thanks to the proportionality between the energy loss of the particle and the inverse of its velocity β, a beam of charged particles slows down while traversing the human body, and progressively releases more energy. There is thus a value of depth in the body that corresponds to the lowest velocity of the particle and its largest energy release: it is the depth of the Bragg peak. After such peak, the beam stops. The main goal of hadrontherapy is to place the Bragg peak in correspondence of the tumor site, in order to irradiate it with the highest amount of energy sparing the surrounding healthy tissues. This can be done by changing the initial energy of the beam, which determines the depth of the peak, as shown in Figure 1.4.

The first problem that needs to be addressed before treatment is the difference between the thickness of the Bragg peak and the dimension of the tumor: most of the times a single Bragg peak is not enough to irradiate the whole cancer volume, thus a Spread Out Bragg peak (SOBP) is needed. By modulating beams with different initial energies and different intensities, one

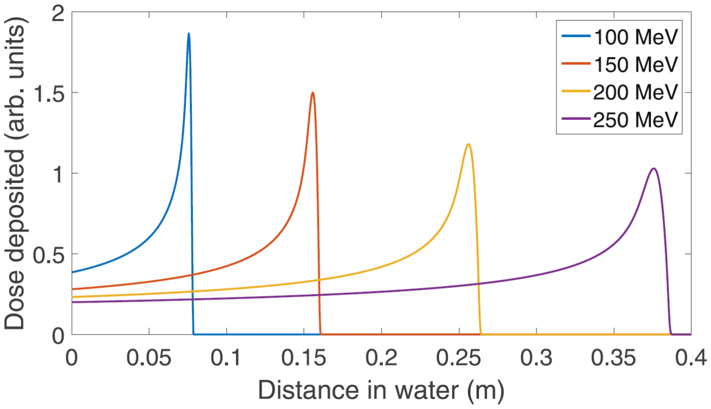

Figure 1.4: Bragg peak for proton beams at different initial energies: the higher the energy, the deeper the position of the peak [7]. With the increase of the depth the peak is less sharp: this is due to an uncertainty that will be described in the following paragraphs.

can obtain a plateau where the energy release is maximum, as illustrated in Figure 1.5, and that can be used to irradiate the whole tumor.

1.1.2 Range

Another important quantity related to the passage of charged particles in matter is the range. This quantity describes how long is the path of a charged particles beam inside a material and provides information about how deep particles can penetrate before losing all of their energy. The particle range relies upon three main parameters, i.e. the type of particle, its initial kinetic energy and the type of material it traverses. Besides these, the concept of range is also strictly connected to the intrinsic statistical nature of the energy loss process: this leads to a spread in the value of dE/dx for a beam of identical particles. According to the thickness of the traversed material, the energy loss distribution can be modeled in two ways: for thin absorbing materials, a Landau-Vavilov distribution can be found, which is a skewed, asymmetric function with a tail at high energies [5]. As the absorber becomes thick, instead, thanks to the central limit theorem, the distribution of energy loss becomes a Gaussian function [6]:

$$f\left(\Delta E\right) = \frac{1}{\sqrt{2\pi\sigma}}\,exp\left(\frac{\left(\Delta E - \overline{\Delta E}\right)^2}{2\sigma^2}\right) \tag{1.3}$$

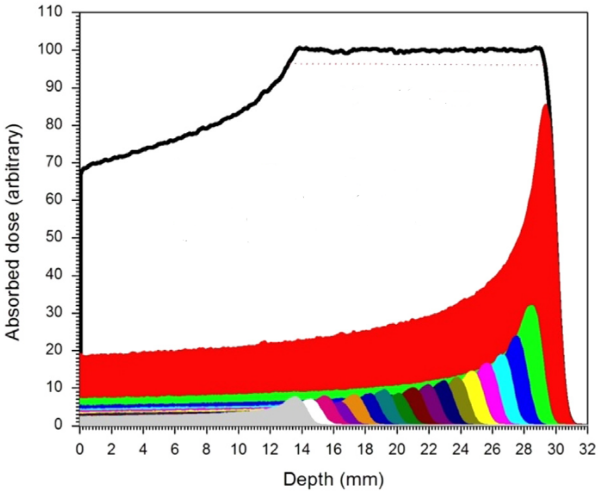

Figure 1.5: Spread Out Bragg Peak obtained from the modulation of several beams with different initial energies and intensities [8]. The obtained plateau (black line) will coincide, during the irradiation, with the thickness of the tumor volume.

The variance of the function depends on the charge of both the incident particle and material, and also on the velocity of the particle. This implies that not only the value of dE/dx, but also the range fluctuates statistically around the mean [9]:

$$R = \int_0^x dx = \int_0^{E_0} \frac{dE}{dE/dx} \tag{1.4}$$

This value represents the most probable and is also called Continuous Slowing Down Approximation (CSDA) range, obtained by neglecting the fluctuations in the energy loss. The behavior affecting both energy loss and range, enclosing their statistical nature, is called *straggling*. From an experimental point of view, the phenomenon of range straggling at a defined energy in a given material can be seen more clearly by taking a beam of charged particles with the desired energy traversing different thicknesses of the material. Then, the ratio of transmitted to incident particles can be measured and plotted as a function of the thickness of the absorber. In the case of an exact process, one would expect a box-shaped function, which drops to zero at the value of the range. What is obtained due to straggling is, instead, summed up in Figure 1.6. Therefore, for small thicknesses all particles of the beam are transmitted, but as the thickness increases there is not a sharp decrease to zero, but a smoother slope down over a certain distribution of thicknesses [5]. The

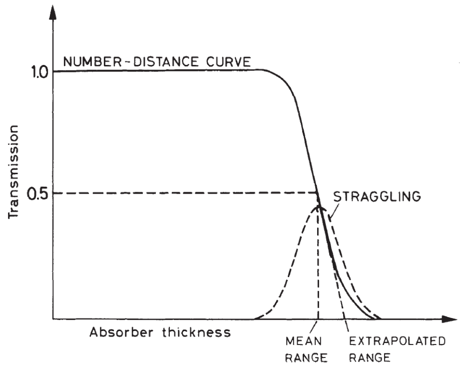

Figure 1.6: Transmission coefficient as a function of depth for a beam of charged particles traversing a material [5]. Due to the statistical nature of the energy loss process, the function is not box-shaped, as one would expect, but has a smooth slope down. This shape of the function allows to define the mean range, where roughly half of the particles are absorbed, and the extrapolated range, where approximately all particles are absorbed.

mean value of this distribution is called *mean range* and it is the thickness at which roughly half of the particles have been absorbed. To obtain instead the thickness at which roughly all particles are absorbed, the *extrapolated range* is used. It can be found by taking the tangent of the curve in the midpoint and extrapolating it to zero. The extrapolated range is the quantity one needs to work with: as a matter of fact, to optimize the therapeutic irradiation, it is necessary to have all particles of the beam stopping at the tumor depth. Both features of the range distribution can be seen in Figure 1.6. In the concept of range lies one of the main uncertainties that affects the use of hadrontherapy. Hence, besides the intrinsic uncertainty caused by straggling, it is also necessary to take into account another contribution. When the therapeutic beam interacts with atoms of the human body, it can create nuclear fragments, i.e. charged particles lighter than the ones composing the beam, that have a longer range with respect to primaries and can thus release energy in tissues deeper than the tumor: this is particularly dangerous if there is an organ at risk close to the area which has to be treated.

1.1.3 Multiple Coulomb Scattering

Up to now, we have assumed that the path travelled by charged particles inside matter can be represented by a straight line, but a more accurate representation of this path is a zig-zag line, which takes into account the

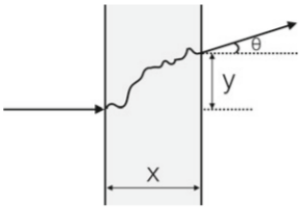

Figure 1.7: Pictorial representation of a charged particle entering a material with a given direction, undergoing multiple coulomb scattering inside the thickness x and exiting with an angle θ and a vertical shift y with respect to its initial direction.

multiple Coulomb scattering contribution. As said before, charged particles traversing matter can also interact with nuclei of atoms in the material, via both electromagnetic and nuclear interaction. When the interaction is electromagnetic, the particle undergoes multiple Coulomb scattering, which is basically a repeated elastic scattering on nuclei of the material. The elastic interaction with electrons has an impact on the energy of charged particles. In the elastic interaction with nuclei, instead, their direction is mostly affected. This is due to the large mass difference between charged particle and nucleus, which makes the energy loss negligible.

Every single scattering, governed by the Rutherford formula [10], adds a small deflection in the beam direction, all the contributions then result in a zig-zag path for the particle, which will exit the material with a deflection θ_0 with respect to its initial direction, as shown in Figure 1.7. When the number of independent scatterings is larger than 20, we can use a statistical approach and find a probability distribution for the net deflection angle as a function of the traversed thickness [5].

In this case, multiple scattering is well described by Moliere's theory [11]. Using a first order approximation, the probability distribution of the deflection angle becomes a Gaussian with mean 0 and a standard deviation given by:

$$\sigma_\theta = \frac{14.1MeV}{\beta pc} Z_p \sqrt{\frac{L}{L_{rad}}} \left[1 + 0.038 \cdot ln\left(\frac{L}{L_{rad}}\right)\right] \tag{1.5}$$

where p is the particle's momentum, β is the velocity, Z_p is the charge of the incident particle and L/L_{rad} is the traversed thickness in terms of *radiation length* [12].

L_{rad} is a parameter that depends on the atomic number and weight of the traversed material [5]:

$$L_{rad} = \frac{716.4\, g/cm^2 \cdot A}{Z\,(Z+1)\, ln\left(287\sqrt{Z}\right)} \tag{1.6}$$

From equations (1.5) and (1.6) it can be seen that multiple scattering increases for thicker materials and that targets containing heavy elements cause larger angular spread than targets containing light elements with the same thickness. Moreover, fixing the type of particle, the scattering decreases at higher energies. Eventually, comparing beams with the same range in water, one can see that the angular spread for protons is about three times larger than the one of ^{12}C ions [6]. The beam spread due to multiple Coulomb scattering in hadrontherapy contains mainly two contributions: one from all the materials in front of the patient, which is dominant at low energies, and another from the tissue between entrance point and stopping depth, dominant at high energies, due to larger penetration depths in tissues.

1.1.4 Nuclear Interaction

Besides the interactions described above, charged particles belonging to therapeutic beams can also produce a nuclear reaction with nuclei of atoms in the material, in this case the human body. The most probable nuclear interaction in hadrontherapy is nuclear fragmentation: according to the size of particles in the beam, which is the projectile, one can observe either target fragmentation, projectile fragmentation or both. The nuclear interaction between charged particles and nuclei of atoms in the human body can be modeled with the abrasion-ablation model, which was introduced by Bowman, Swiatecki and Tsang in 1973 [13]. This model splits the fragmentation process in two stages. The abrasion stage can be seen as a particle removal in the ion-ion interaction, while ablation is a nuclear de-excitation, i.e. a consequence of the first stage. The model for the interaction is illustrated in Figure 1.8: once the projectile nuclei, which move at relativistic speeds, arrive, they collide with stationary target nuclei and there is an overlap between projectile and target. This creates a *fireball*, whose size depends on the impact parameter of the collision. Peripheral collisions, which have a small impact parameter and are also the most common ones in the hadrontherapy energy range, i.e. [60-400] MeV/u, cause a small overlap, while in central collisions the total destruction of nuclei can take place, due to a much larger overlap of projectile and target. The portion of overlapped nuclear material is sheared away in the abrasion step: as a result, a highly excited pre-fragment is formed. In the second phase of the process, i.e. ablation, large pre-fragments

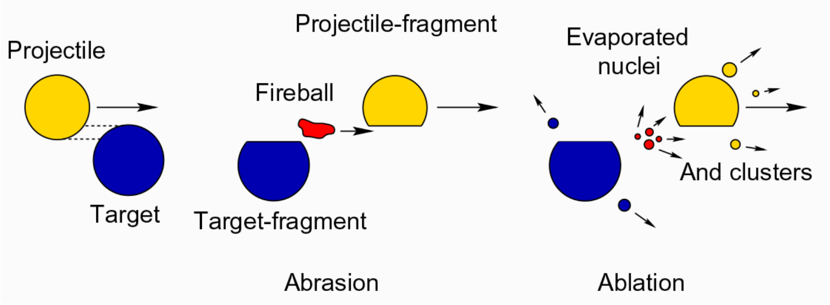

Figure 1.8: Schematizing of the nuclear fragmentation process in three phases: on the left, projectile and target right before the collision, in the center the abrasion stage and on the right the final stage, i.e. ablation.

created by the abrasion phase de-excite and, in doing so, they lose energy by evaporating nucleons or light particles and emitting photons. The resultant products of the collision, sometimes referred to as secondary products, are the nuclear fragments. Target nucleons that are not hit by the projectile remain stationary and projectile nucleons not taking part to the reaction proceed with their initial velocity.

Nuclear fragmentation usually produces two different outcomes: when the projectile is a proton, the beam energy is not enough for projectile fragmentation, thus only target fragmentation is produced. This is the case of proton therapy. When the projectile is a heavier particle, instead, also projectile fragmentation can take place, which is what happens for ^{12}C therapy. Both types of reactions create some physical effects that have to be taken into account in the context of therapy, to be able to evaluate their consequences on the patient and obtain an effective treatment.

Target Fragmentation

In the case of proton therapy, projectile nuclei do not have enough energy to beak up into quarks, thus fragmentation only occurs in the target: as mentioned before, this implies the creation of very slow fragments, with short range and high energy release, as listed in Figure 1.9. The main concern about these fragments is their biological effect in the entrance channel, i.e. the portion of the human body before the Bragg peak, where ionization of the DNA of cells is unwanted and could be dangerous, due to the presence of healthy tissues. Moreover, plot 1.10 shows the percentage of ionization (green) and fragmentation (red) events in the irradiation with charged particles. In the Bragg peak area the higher contribution comes from ionization,

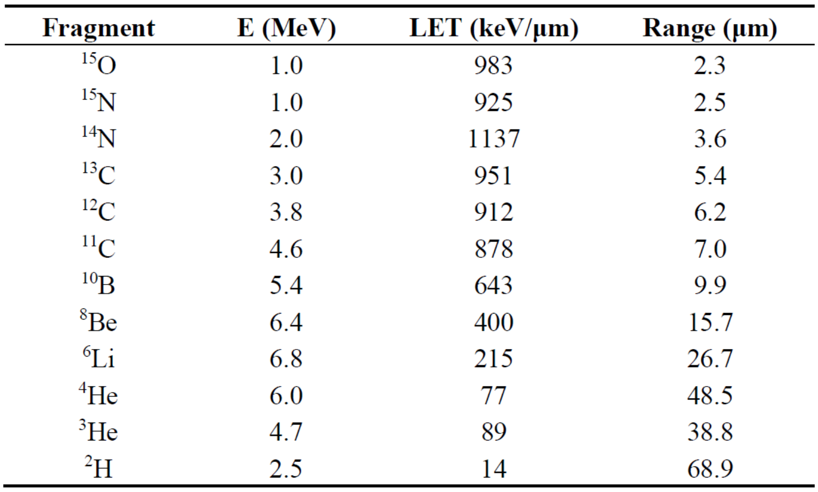

Fragment	E (MeV)	LET (keV/µm)	Range (µm)
^{15}O	1.0	983	2.3
^{15}N	1.0	925	2.5
^{14}N	2.0	1137	3.6
^{13}C	3.0	951	5.4
^{12}C	3.8	912	6.2
^{11}C	4.6	878	7.0
^{10}B	5.4	643	9.9
^{8}Be	6.4	400	15.7
^{6}Li	6.8	215	26.7
^{4}He	6.0	77	48.5
^{3}He	4.7	89	38.8
^{2}H	2.5	14	68.9

Figure 1.9: Expected target fragments produced by a 180 MeV/u beam of protons in water. For each fragment, the expected energy, energy transfer and range are listed [14].

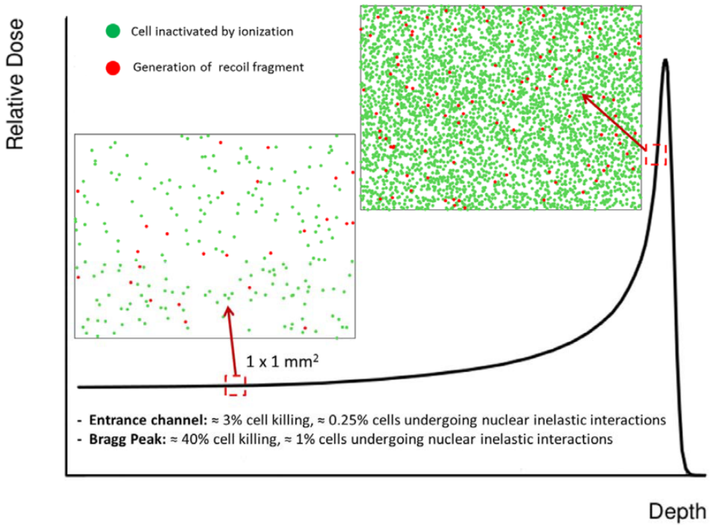

Figure 1.10: Schematic view of the impact of ionization (green dots) and target fragmentation (red dots) along the track of the charged particle, in tissue sections of 1x1 mm^2. As opposed to the Bragg peak, where damage to cells is wanted, in the entrance channel the action of target fragments might be dangerous [14].

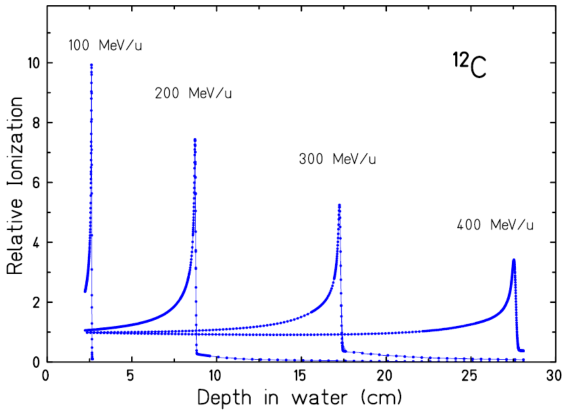

Figure 1.11: Measured Bragg curves for carbon beams at different initial energy. Unlike the case of protons, after the peak there is a dose tail increasing with initial energy [6].

and both types of event have an advantageous effect on tumor cells. In the entrance channel, i.e. the region constituted by healthy tissues, there is instead a higher proportion of nuclear reactions, which could produce unwanted effects. For all the reasons explained above, it is necessary to deeply understand the behavior of nuclear fragments inside the human body, to be able to exploit proton therapy in the safest way possible. Nowadays, though, there is a huge lack of experimental data regarding target fragments, because their very short range makes it impossible for them to exit the target and prevents their detection. The FOOT experiment works precisely in this context: its main goal is to measure the double differential cross section, with respect to the fragment's kinetic energy and emission angle, for the production of target fragments in the interaction between the therapeutic beam and the patient. Due to the very short range of fragments, the technique of *inverse kinematics* described in Chapter 2 is needed.

Projectile Fragmentation

The work of the FOOT experiment will also be useful to obtain a deeper knowledge of projectile fragmentation, which only happens in heavy-ion hadrontherapy. In this case nuclear fragments create a tail of energy release after the Bragg peak, as shown in Figure 1.11 for beams of ^{12}C hitting a water target at different initial energies.
Such tail can be a drawback in cases where an Organ At Risk (OAR), i.e. an

organ that is particularly close to the tumor and could be damaged by the irradiation, is present: one thus needs to know its effect in the most precise way possible. Unlike the case of target fragmentation, where the flux of the therapeutic beam remains approximately the same, projectile fragmentation in beams of heavy ions leads to an attenuation of the primary beam's flux and a build-up of secondary fragments with lower charge, which are the cause of the tail beyond the Bragg peak [15].
Thanks to the different behavior of projectile fragments with respect to target's ones, some experimental measurements have been possible and the primary beam attenuation and fragment buildup can be estimated with good accuracy by detecting the charged fragments produced as a function of the thickness of traversed material. Haettner et al. [15] measured the charge, mass and exit angle of charged fragments produced by a beam of ^{12}C, which is the most common isotope for heavy ion hadrontherapy, with two different energies and at different depths in water. Water is commonly used in this kind of measurements because it is the predominant constituent of the human body [6].

The plot 1.12 of beam attenuation and the correspondent Bragg curve at 200 and 400 MeV/u show that, at 200 MeV/u, 70% of the primary carbon ions are still present at Bragg peak position, while at 400 MeV/u the fraction of surviving primary ions is only 30%. This results in a lower and less sharp Bragg peak at higher energy and, subsequently, a larger tail after the peak.
Another interesting plot in Haettner's study is the build-up of charged fragments as a function of depth in water: it is obtained by integrating the angular distribution of each fragment between 0° and 10°.

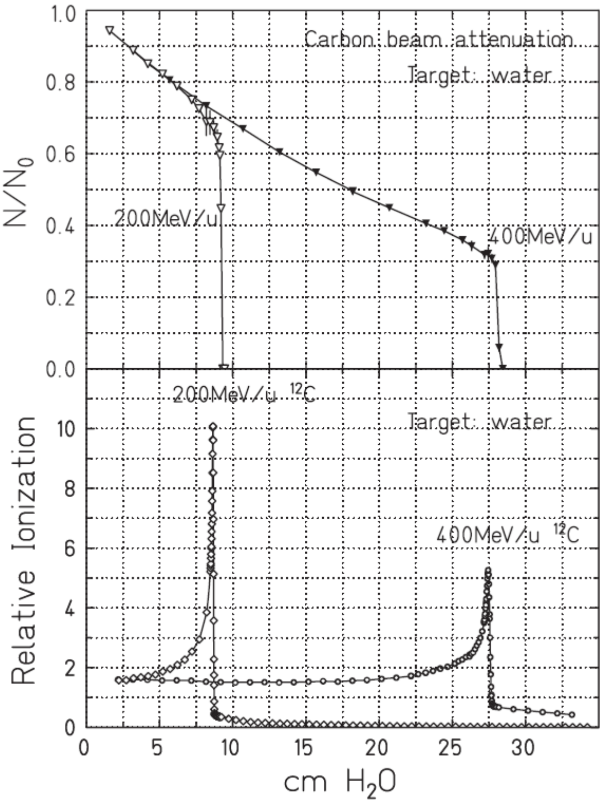

Figure 1.12: Surviving fraction of ^{12}C nuclei as a function of depth (figure above) in water and their corresponding Bragg curves (figure below). The two represented carbon beams have, respectively, initial energy of 200 and 400 MeV/u [15].

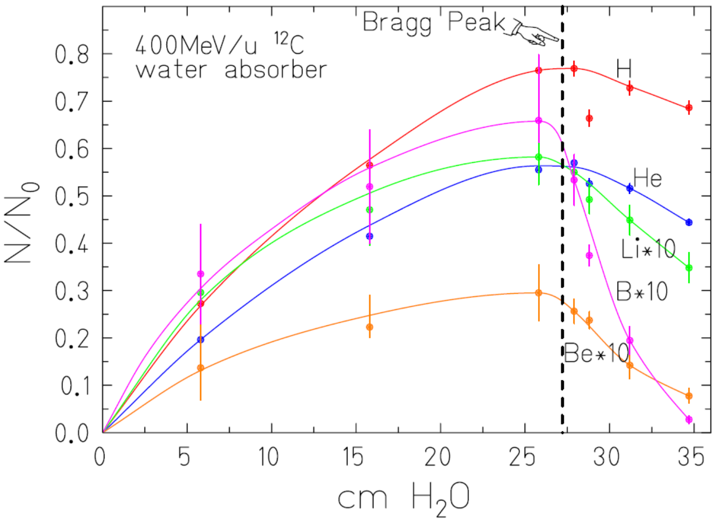

Figure 1.13: Build-up of charged projectile fragments as a function of depth in a water target, for an impinging carbon beam with 400 MeV/u energy. The dashed line shows the depth of the Bragg peak, beyond which the majority of fragments are light (Z=1,2) [6].

Plot 1.13, representing the build-up for a primary beam of 400 MeV/u, shows that few centimeters after the Bragg peak the predominant fragments are the lightest ones, i.e. protons and alpha particles, which also have larger emission angles. Heavier fragments, instead, are usually emitted in a more narrow cone, between 0° and 5°.

The energy of 400 MeV/u is more or less the highest value required for heavy ion therapeutic beams and it is the energy at which fragmentation effects are the most significant. As the nuclear cross section does not vary much in the range between 100 and 400 MeV/u, plot 1.13 can also be used to make reliable predictions about projectile fragments produced by primary beams with lower energies [15].

1.2 Radiobiology

To have a more complete knowledge of what hadrontherapy is, together with its advantages and drawbacks, not only the physical aspect should be considered. The fact that charged particles during therapy interact with living tissues must be taken into account to evaluate the effects of hadrontherapy in the most complete way possible, thus also from the biological point of view.

For this purpose, *radiobiology* is very helpful: it is a branch of science which combines principles of physics and biology, describing the effect of ionizing radiation on living organisms by using some dedicated quantities and mechanisms.

In the specific case of hadrontherapy, which is an irradiation of a localized volume in the human body affected by cancer, the biological effect stands mainly in the ionization of cells' DNA, which allows to kill them or prevent their multiplication.

Usually, cells can be damaged in two ways: *direct* or *indirect*. In the first case, the energy released by charged particles in the therapeutic beam produces some harm in the living tissue. In the second case, instead, charged particles interact with molecules of the human body, mainly water, producing free radicals, i.e. highly reactive molecules that can then damage cells.

In the context of cancer treatment, radiobiology helps to understand the risk-benefit ratio of a specific therapy: therefore, with some particular parameters, one can evaluate the damage caused to cancerous and healthy cells, the advantage in using charged particles instead of photons and how much radiation of each type is needed for the patient, based on where and how extended the cancer is.

1.2.1 Dose

A very important quantity for the description of the irradiation in hadrontherapy is the dose. It is defined as:

$$D = \frac{dE}{dm} \tag{1.7}$$

thus it is the energy released by a beam of particles per unit mass of the traversed material. The SI unit measurement for dose is Gray (Gy), which corresponds to J/kg.

For every type of radiation, the amount of released dose changes with depth in matter and depends on the initial energy of the beam and on the velocity of particles. Studying the variation of the dose, the depth-dose curve can be obtained. It has a very characteristic shape for neutral and charged particles. The plot in Figure 1.14 helps understanding the difference between conventional RT and hadrontherapy: the former has the major dose release at low depths, i.e. on the surface of the human body. With the latter, instead, the initial energy of the beam can be adjusted in order to place the largest energy release, i.e. the SOBP, at the depth where the tumor is. In this way, the tumor receives the largest dose, and the surrounding healthy tissues are mostly spared.

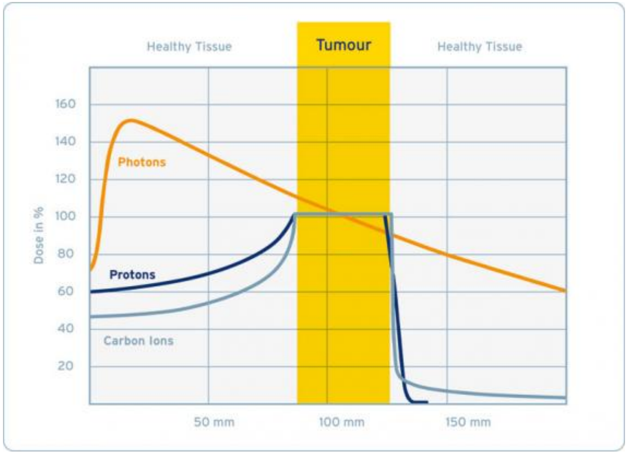

Figure 1.14: Dose released by photons (orange line), protons (blue line) and carbon ions (gray line) as a function of depth in the human body. Photons and charged particles have a very different shape of the depth-dose profile, also called Bragg curve.

Unfortunately, dose does not take into account the biological aspect of the energy release: 1 Gray of photons produces a different biological damage with respect to 1 Gray of protons. At the same time, 1 Gy of a given radiation can have very different effects on different types of tissues. This is the reason why *equivalent* and *effective* dose (i.e. D_{eq} and D_{eff}, respectively) need to be introduced.

$$D_{eq} = \sum_R w_R D \tag{1.8}$$

$$D_{eff} = \sum_T w_T D_{eq} \tag{1.9}$$

Equations (1.8) and (1.9) contain two factors used to weigh the dose: w_R depends on the type of radiation traversing the tissue, while w_T depends on the type of tissue that is being irradiated: the typical values for both factors are listed in figure 1.15. Once the biological effect of radiation is taken into account, the unit of measurement changes from Gray (Gy) to Sievert (Sv). While 1 Gy of photons and protons can cause very different biological damage, a 1 Sv dose has the same biological effect independently from the particles that have caused it.

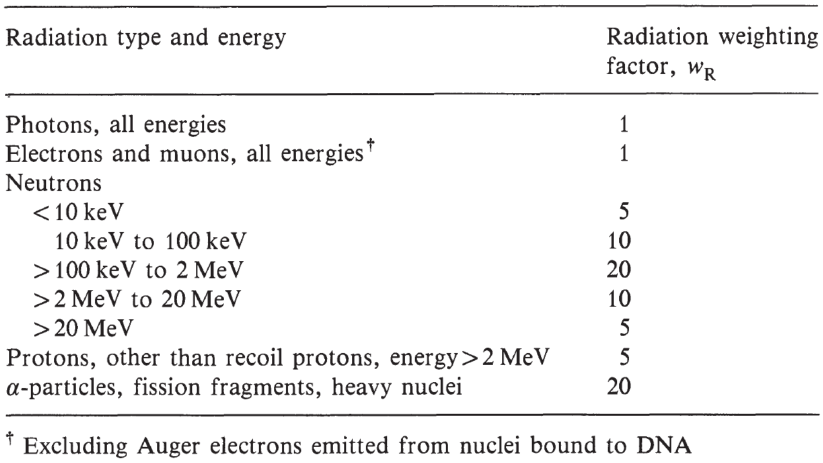

Radiation type and energy	Radiation weighting factor, w_R
Photons, all energies	1
Electrons and muons, all energies[†]	1
Neutrons	
<10 keV	5
10 keV to 100 keV	10
>100 keV to 2 MeV	20
>2 MeV to 20 MeV	10
>20 MeV	5
Protons, other than recoil protons, energy >2 MeV	5
α-particles, fission fragments, heavy nuclei	20

[†] Excluding Auger electrons emitted from nuclei bound to DNA

(a) Typical weighing factors for radiations

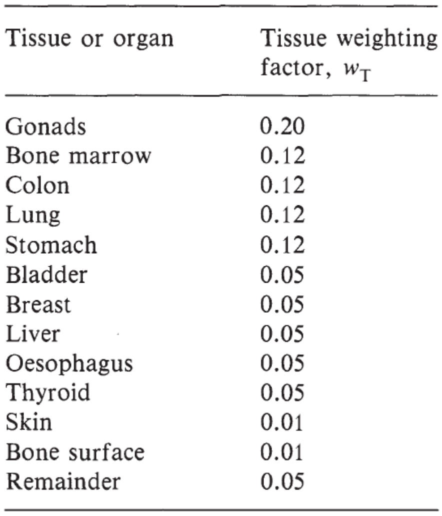

Tissue or organ	Tissue weighting factor, w_T
Gonads	0.20
Bone marrow	0.12
Colon	0.12
Lung	0.12
Stomach	0.12
Bladder	0.05
Breast	0.05
Liver	0.05
Oesophagus	0.05
Thyroid	0.05
Skin	0.01
Bone surface	0.01
Remainder	0.05

(b) Typical weighing factors for tissues

Figure 1.15: Tables containing the typical values of (a) w_R used to weigh the type of radiation in the equivalent dose and (b) w_T for the type of irradiated tissue in the effective dose [5].

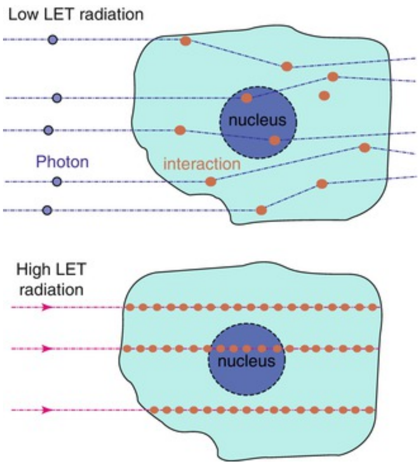

Figure 1.16: Schematic representation of energy releases caused in cells by low and high LET radiations. In the first case, sparse interactions have much smaller probability to create severe damage with respect to the second case, where interaction are denser and more frequent.

1.2.2 LET

Another important parameter, mainly used to characterize the track left by a particle, is the *Linear Energy Transfer* (LET):

$$LET = \frac{dE}{dl} \tag{1.10}$$

It can be defined as the average energy released per unit length. At first sight, the definition of LET is the same as the one used for the stopping power (1.1). But while the stopping power focuses its attention on the energy loss by a charged particle moving through a medium, the LET is focused on the rate of energy absorption by the medium, as the charged particle traverses it [16]. It is also typically focused on the ionization released close to the track of the particle, excluding all secondary particles with longer range. Moreover, the unit measurements are different: for stopping power, MeV/cm are used, while LET is expressed in $keV/\mu m$.
According to its LET value, each type of radiation can be classified as *sparsely* or *densely* ionizing. Photons are classified as sparsely ionizing, protons and heavier charged particles as densely ionizing. The denser the ionization by the particle, the higher the probability to create a significant damage in the DNA of tumor cells, as schematized in Figure 1.16.

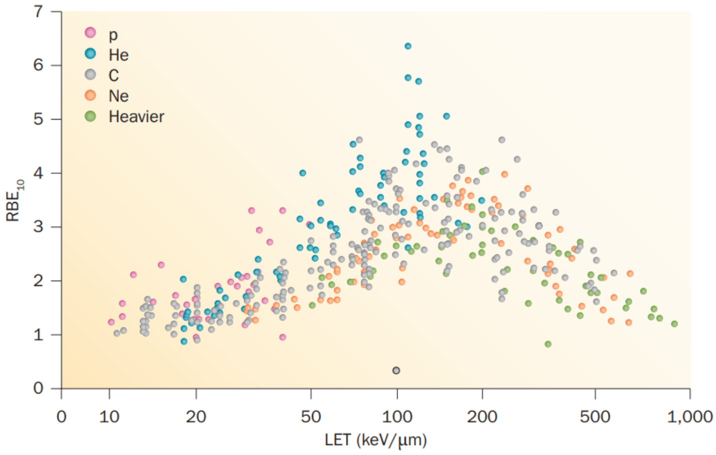

Figure 1.17: Variation of the RBE value as a function of LET for different types of charged particles [17].

1.2.3 RBE

Besides the advantageous depth-dose profile, another powerful feature of protons and heavier charged particles is the enhanced biological effect with respect to photons, which is given by the more severe damage caused to DNA of cells. For an accurate estimation of the efficacy of ions with respect to photons, the concept of Relative Biological Effectiveness (RBE) must be introduced [6]:

$$RBE = \left.\frac{D_{x-rays}}{D}\right|_{isoeffect} \tag{1.11}$$

The RBE of a given radiation is the ratio between the dose of x-rays and the dose of such radiation, respectively referred to as D_{x-rays} and D in equation (1.11), needed to produce the same biological damage.

From the formula (1.11) it is clear that protons, ^{12}C ions and all charged particles will have a RBE larger than 1. Since charged particles release more energy in matter with respect to photons, RBE will also be connected to the LET of particles, as shown in figure 1.17. The RBE depends on many factors concerning the treatment: biological endpoint, dose, type of irradiated tissue, particle type and energy. Considering it as a constant value it is a simplification, because the RBE of the same particle can vary drastically within the tumor volume and the treatment field.

Moreover, once the primary beam used for the irradiation undergoes fragmentation, the combined biological effect of beam and secondary fragments must be taken into account.

Currently, hadrontherapy has no Treatment Planning System (TPS) able to evaluate the RBE of beams and their produced fragments [2]: hopefully, with measurements from the FOOT experiment, this contribution can be implemented to create an automated TPS for therapy.

1.3 Hadrontherapy

A further difference between conventional radiotherapy and hadrontherapy lies in their history: hadrontherapy is a much “younger” type of treatment, due to the later and not yet complete discovery of its physical effects on matter and, subsequently, on the human body. A very detailed report of how hadrontherapy was born and developed can be found in the paper *History of hadrontherapy* by Ugo Amaldi [18].

Reminding that a hadron is any type of particle composed by quarks and bound by strong force, we know that the first type of hadrontherapy involved neutrons and it began in the 1930s in the USA. The idea of using the Berkeley cyclotron for medical purposes came from Ernest Lawrence, who worked together with his brother John and, after performing some experiments, in 1938 began treating the first patients using neutron beams.

The study was carried on in the following years by doctor Robert Stone, who treated approximately 200 patients. Due to the primitive techniques and the fact that the bad consequences on healthy tissues were much higher than the benefits of the therapy, the use of neutrons was dismissed in 1948.

The pioneer of proton therapy was Robert Wilson, one of Lawrence’s students. He first exposed his idea of using protons to cure cancer in 1946, in his paper “*Radiological use of fast protons*”, using as a motivation for therapy the advantageous depth-dose profile of charged particles and the Bragg peak (see Section 1.1.1).

The first patient was treated in 1954 at the Lawrence Berkeley Laboratory: beams of protons were managed in the same way as beams of photons, so at first their electric charge was not exploited in the beam creation and in the beam handling. With the years, more laboratories started to cure patients using protons. The main drawback of treatments performed in the first years of hadrontherapy is that they were carried on inside facilities mainly dedicated to experimental physics: for this reason, there were no machines devoted to imaging and diagnostics, thus it was difficult to monitor the tumor irradiation, the surrounding tissues and the evolution of the patients’ situation. It took about twenty years to go from physics laboratories to more equipped hospital-based facilities: the first ones were built in California and Japan, starting their work in, respectively, 1990 and 2000.

In the mean time, thanks to the combined work of radiation oncologists and physicists, it was discovered that proton therapy is particularly useful and advantageous in the control of tumors that are close to organs at risk.

In the following years, one more hypothesis took place: heavier ions, that have less lateral spread and straggling with respect to protons, could also be used for cancer therapy. After several trials, having to combine a large dose release and small side effects in normal tissue, Yasuo Hirao and his collaborators chose to exploit carbon ions. In Japan, the HIMAC (Heavy Ion Medical Accelerator in Chiba) facility was built and the first patient was treated in 1994, using a beam of carbon ions with less than 400 MeV/u. By the end of the XX century, Europe also decided to invest on hadrontherapy with carbon, and a carbon ion facility was built at GSI, in Germany. The first treatment was performed in 1997. Up to now, more and more hospitals have decided to invest on hadrontherapy with protons, carbon or both. Nowadays, though, hadrontherapy is only used as an alternative to conventional RT in the most difficult or extreme cases, due to the much higher cost of the required equipment and treatment planning and to the partly unknown underlying physical processes, such as target fragmentation.

A very useful source of information is the Particle Therapy Cooperative Group (PTCOG), which was created in the '80s for scientists to exchange ideas for the development of HT. The PTCOG is still active and every year it provides a report of all the particle therapy facilities in the world and the number of patients treated up to now. According to their website [19], by the end of 2020 more than 100 facilities were active with more than 290000 patients treated, the majority of them using protons. The trend of the number of treated patients in the last 13 years is shown in Figure 1.18 for protons and carbon ions. In Italy, hadrontherapy is performed in three facilities. At the Protontherapy Center in Trento, a hospital-based building which only uses protons, at CNAO (Centro Nazionale di Adroterapia Oncologica) in Pavia, hospital-based and equipped with a synchrotron that allows treatments with protons and ^{12}C ions, and at the INFN LNS (INFN-Laboratori Nazionali del Sud) in Catania, a laboratory-based facility which is specialized on eye tumors treatment with protons.

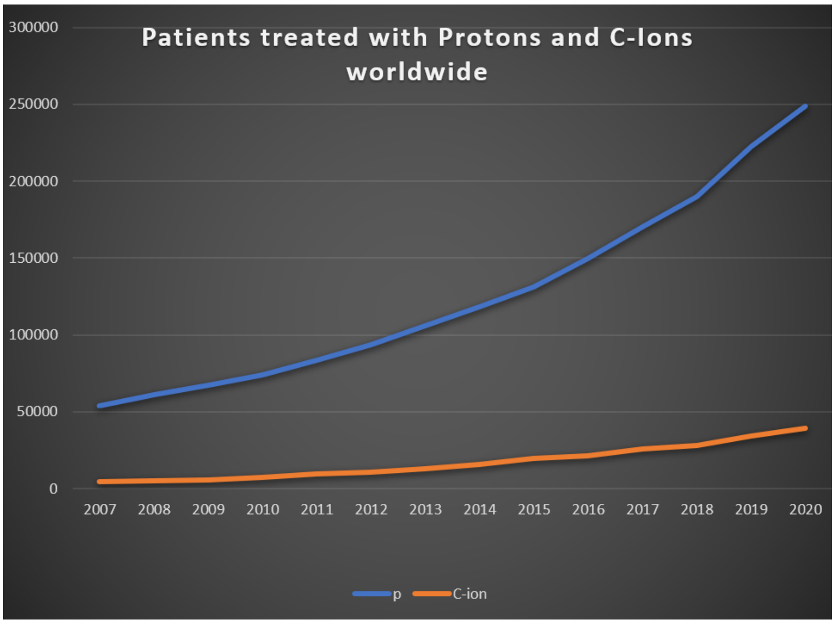

Figure 1.18: Progress of the number of patients who received a HT treatment, from 2007 to 2020, worldwide. The blue line shows a quite sharp increase of proton treatment, while the orange line shows the slower increase of carbon treatments [19].

1.4 Space Radioprotection

Despite dealing with quite different situations, there is an important overlap between the physics of hadrontherapy and radioprotection in space, which are both part of the measurements campaign program of the FOOT experiment. Energetic particles in space come mainly from three sources: Solar Particle Events (SPEs), Galactic Cosmic Rays (GCRs) and geomagnetically trapped particles. SPEs are mainly composed by protons emitted from the Sun during coronal mass ejections and solar flares. They have an energy spectrum that can reach the GeV region and they are unpredictable, thus risking to deliver a lethal dose to astronauts. GCRs consist of high energy protons and highly energetic charged particles (HZE) that are produced by supernovae in the Milky Way, outside of the solar system. GCRs are fully ionized nuclei and their isotopic composition is known: 85% of protons, 14% of alpha particles, 1% of heavier ions (with carbon ions among the most abundant). Their energy ranges between few MeV to about 10^{20} eV, but the peak in the energy spectrum is in the hundreds of MeV to GeV range [20], as reported in figure 1.19. This is also the energy range of initial beam energies for particle therapy. Lastly, geomagnetic trapped particles consist of protons and electrons, confined by the Earth magnetic field into two regions, called Van Allen belts. The inner belt contains protons with energies up to 100 MeV, while in the outer one there are electrons with energy up to 100 keV. Trapped particles are not a concern for deep space explorations, which usually happen outside of Earth's magnetosphere, i.e. the area in which such particles are confined. In long duration space missions, the dominant radiation risks are thus the ones from GCRs ans SPEs. The contribution of these two risks is not equal. As a matter of fact, SPEs occur on a cycle, with roughly seven events per year, and the most dangerous ones which could have severe effects on the human body only happen once or twice in a millennium. Nevertheless, their contribution should not be neglected, even if predictions on SPEs are very hard to obtain. GCRs instead, are an isotropic type of radiation that continuously reaches the spaceship hull. The goal of space radioprotection is to minimize the dose that enters the spacecraft: to do so, the most efficient technique is to build a shield that is able to reduce the flux of incident particles. Once the incident particles traverse the shielding material, though, nuclear fragmentation takes place, modifying the composition of space radiation spectra. This is the same phenomenon that takes place when an hadrontherapy beam enters the human body and that needs to be accounted for in the calculation of the biological effect of radiation. For this reason, it is important to obtain dose estimations that take into account the fragmentation of primary radiation: this can be done by direct measurements, but the most efficient tool nowadays is

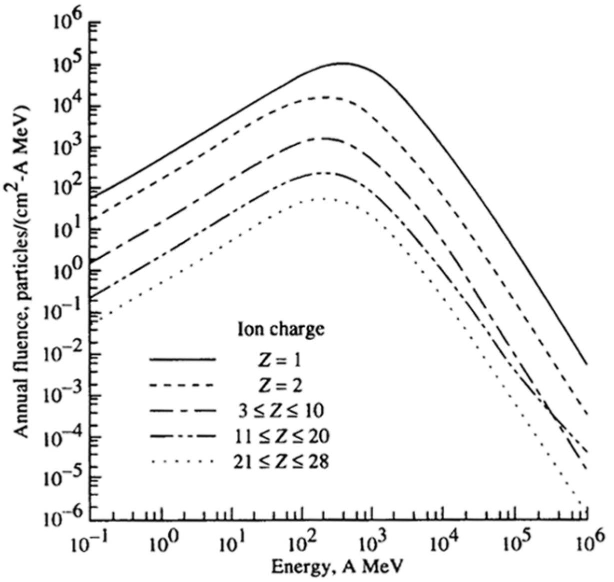

Figure 1.19: Annual fluence of charged ions belonging to GCRs as a function of their energy [21].

calculation through deterministic and Monte Carlo transport codes. In this context, a fundamental element for validating and benchmarking the codes is the cross section measurements describing nuclear fragmentation of primary ions on several shielding materials [2]. Moreover, experimental studies have shown that, thanks to their high mass stopping power, light materials are the best candidates for shielding, especially the ones which are rich in hydrogen [22]. This leads to a further element in common with hadrontherapy, i.e. the target material.

Summing up, the particle species that are currently used for hadrontherapy or considered promising alternatives (protons, carbon and helium ions) are also among the most abundant species in space. The overlap is also in terms of targets, energy range of interest and physical processes taking place: this is the reason why nuclear fragmentation cross sections measured by the FOOT experiments can be of great help to evaluate the dose received by the fly crew and the electronics during long-lasting space mission (i.e. Mars exploration).

Chapter 2

The FOOT (FragmentatiOn Of Target) Experiment

The FOOT (FragmentatiOn Of Target) experiment works in the context of applied nuclear physics: its main goal is to perform precise measurements of differential fragmentation cross sections, with respect to kinetic energy and production angle of emitted nuclear fragments. The experiment has been approved and funded by INFN (Italian National Institute of Nuclear Physics) in 2017 and nowadays the collaboration includes about one hundred physicists from Italy, Germany, France and Japan, working at universities and research centers. The final goal of the experiment is the measurement of the fragmentation cross section with a maximum uncertainty of 5% and the fragments energy spectrum with an energy resolution of the order of 1-2 MeV/u. The results will lead to a more precise treatment planning system (TPS) for hadrontherapy, will help in benchmarking models of nuclear interactions and in the design and optimization of spacecraft shielding for long duration space missions.
The FOOT apparatus foresees two different setups: the magnetic spectrometer used to identify fragments heavier than Helium and the emulsion spectrometer optimized for light fragments. The electronic setup is currently in the final construction phase, which began in 2018, while the emulsion spectrometer has already began taking data in its final configuration, with two experimental campaigns at GSI research center, in 2019 and 2020. Despite not being complete, most parts of the magnetic spectrometer have been tested and calibrated with several data takings at CNAO (Pavia, Italy), GSI (Darmstadt, Germany) and TIFPA (Trento, Italy).
This chapter will be completely dedicated to the FOOT experiment: in section 2.1, the motivations and research program of FOOT are outlined; section 2.2 contains an explanation of the inverse kinematic technique; section 2.3

lists the design criteria of the apparatus; sections 2.4 and 2.5 are dedicated to a description of the magnetic spectrometer and its data acquisition system; finally, section 2.6 delineates the structure of the emulsion chamber.

2.1 Motivations and Research Program

As already mentioned in chapter 1, the overall effect of nuclear fragmentation is a modification of the delivered dose in the patient's body with respect to the one only due to primary ions radiation [2]. Treatment planning systems (TPS) are not yet able to completely reproduce this modification of the radiation field. As a matter of fact, TPS are mostly based on nuclear models and MC simulations, but there are very few cross section values available for fragmentation. In recent years, some experiments have been performed to investigate projectile fragmentation in ^{12}C ion beams, but the studied initial energies and targets were very few [24, 25, 26]. The process of target fragmentation, instead, has been practically neglected up to now, due to the intrinsic difficulty in the detection of produced fragments, which have extremely low energy and therefore very short (μm) range. The same delivered dose modification happens when charged particles of the spatial environment hit the shielding of spaceships, thus the charged particles that reach astronauts and electronic equipment inside the spaceship are the results of fragmentation: the physical process is analogous, but the initial beam energy is higher, typically ∼700 MeV/u. The FOOT experiment has been designed to detect, track and identify all the charged fragments produced in ion collisions with different targets, with the aim of measuring both projectile and target fragmentation. The goal is to measure the double differential cross section (with respect to kinetic energy and solid angle) with an accuracy $< 5\%$: this reflects into a quite strict isotopic identification ability. More specifically, the clear separation of analysed isotopes needs an accuracy of 2-3% for charges and 5% for masses. The measurement of target fragmentation will need an *inverse kinematic* approach to be achieved: it will be described in detail in the following. FOOT has been designed as a fixed target experiment: the initial energies of beams will be 200 MeV/u for hadrontherapy applications and 700 MeV/u for space radioprotection. Thanks to the compatibility between the ions composing projectile and target, the only in which the two applications will difference is the initial energy. The main targets of interest have been chosen according to the most abundant elements in the human body: carbon, oxygen and hydrogen. The experiment will not make use of a pure gaseous hydrogen target, due to its low density, which implies low interaction rate, and the risk in handling it in therapy and research centers

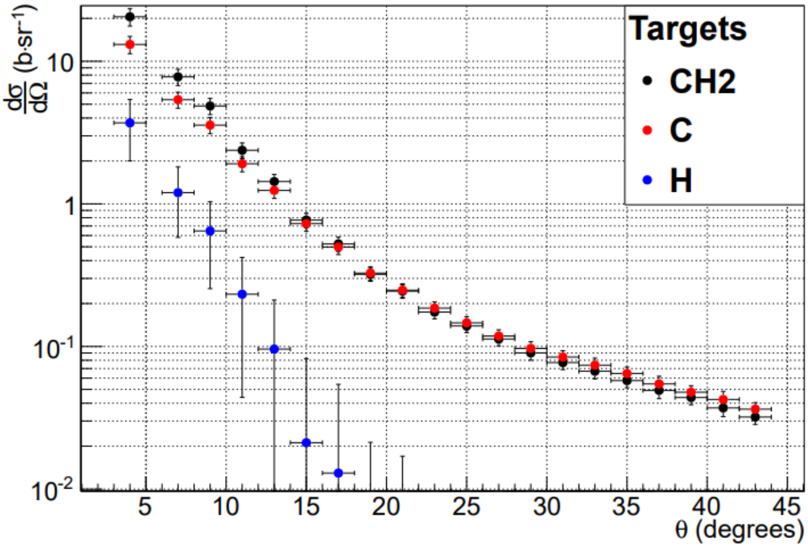

Figure 2.1: Combination of the carbon and CH_2 angular distribution to determine the hydrogen angular distribution for alpha fragments. The angular distribution for the hydrogen target is the difference between the CH_2 and carbon target, divided by two [27].

where the experiment will be held. To overcome this difficulty, an alternative procedure has been chosen: it has already proven to be feasible, as reported in [27] and shown in figure 2.1. Using a multi-layer composite target of C_2H_4 and C, the p-N cross section can be obtained by subtraction:

$$\frac{d\sigma}{dE_k}(H) = \frac{1}{4}\left(\frac{d\sigma}{dE_k}(C_2H_4) - 2\frac{d\sigma}{dE_k}(C)\right) \tag{2.1}$$

$$\frac{d\sigma}{d\Omega}(H) = \frac{1}{4}\left(\frac{d\sigma}{d\Omega}(C_2H_4) - 2\frac{d\sigma}{d\Omega}(C)\right) \tag{2.2}$$

where E_k indicates the kinetic energy and Ω the solid angle of the emitted fragments. The main drawback of this technique is that the uncertainty for the cross section of hydrogen will be the quadratic sum of uncertainties for each target, thus it will be affected by a quite large error.

2.2 Inverse Kinematic Approach

The choice of an inverse kinematic technique comes from the need to overcome the difficulty of short range of target fragments, which are not able to exit even a thin target material and would therefore be impossible to detect. Moreover, the use of a thinner target would imply a very low interaction rate, thus the need of a very large time for data acquisition, together with the difficulty to handle the target without damaging it. Therefore, while in a direct kinematic layout one would have a beam of protons hitting a target of tissue-like material (^{12}C,^{16}O), the situation must be inverted. In an inverse kinematic framework, a tissue-like beam hits a hydrogen-rich target. If the kinetic energy per nucleon remains the same, to go from the *patient reference frame* (proton projectile + tissue-like target) to the new *laboratory reference frame* (tissue-like projectile + proton target), a Lorentz boost will be sufficient. A Lorentz boost is a coordinates transformation between two inertial reference frames, one moving with velocity β with respect to the other. In this specific case, the beam moves along the z axis. The laboratory frame can be indicated as S and the patient's frame as S'. S = ion moving with β along z, proton at rest; S' = ion at rest, proton moving with $-\beta$ along z. The four-momentum of the ion in S is **P**=(E/c, $\vec{p}$) and the four-momentum of the proton in S' is **P'**=(E'/c, $\vec{p'}$). Using the Lorentz boost formula, the 4-momentum coordinates in S' can be written as:

$$\frac{E'}{c} = \gamma\left(\frac{E}{c} - \beta p_z\right) \tag{2.3}$$

$$p'_x = p_x \tag{2.4}$$

$$p'_y = p_y \tag{2.5}$$

$$p'_z = \gamma\left(-\beta\frac{E}{c} + p_z\right) \tag{2.6}$$

Then, expressing the transformation in a matrix form:

$$\mathbf{P'} = \mathbf{\Lambda P} \tag{2.7}$$

$$\begin{pmatrix} E'/c \\ p'_x \\ p'_y \\ p'_z \end{pmatrix} = \begin{pmatrix} \gamma & 0 & 0 & -\beta\gamma \\ 0 & 1 & 0 & 0 \\ 0 & 0 & 1 & 0 \\ -\beta\gamma & 0 & 0 & \gamma \end{pmatrix} \begin{pmatrix} E/c \\ p_x \\ p_y \\ p_z \end{pmatrix} \tag{2.8}$$

The inverse Lorentz transformation can therefore be written as:

$$\mathbf{P} = \mathbf{\Lambda^{-1} P'} \tag{2.9}$$

and the inverse matrix can simply be obtained by changing the sign of β.

$$\Lambda^{-1}(\beta) = \Lambda(-\beta) = \begin{pmatrix} \gamma & 0 & 0 & \beta\gamma \\ 0 & 1 & 0 & 0 \\ 0 & 0 & 1 & 0 \\ \beta\gamma & 0 & 0 & \gamma \end{pmatrix} \tag{2.10}$$

In order to correctly apply the Lorentz boost, the accuracy on the emission angle measurement must be of the order of mrad, for both the projectile and the target. The recommended target thickness to have a good interaction rate and minimize the secondary fragmentation, which also allows the correct accuracy, is 2-4 mm.

2.3 Apparatus Design Criteria

The constraints on the design and optimization of the apparatus have been set with the help of a Monte Carlo (MC) simulation of a ^{16}O beam impinging on a polyethylene target at 200 MeV/u. The simulation has been performed using the FLUKA code [28, 29] and the resulting distributions of fragments yield are reported in figure 2.2 for exit angle (left) and kinetic energy (right). The kinematics of the fragmentation reaction causes fragments to exit with different angles: heavy ($Z \geq 3$) fragments are mostly forward-peaked and, in general, emitted within a cone of 10° semiaperture with respect to the beam axis [30], while light fragments can have much larger exit angles. Moreover, the kinetic energy per nucleon is peaked around the beam value for heavy fragments, while light fragments have wider kinetic energy distributions. The aforementioned features of fragments must therefore be considered in designing the apparatus.
Another aspect to take into account is that the detector must be movable and easily fit in the experimental rooms of centers providing the beam at therapeutic energies. Being FOOT a fixed target detector, the automatic choice would be a magnetic spectrometer. The size, cost and weight of a magnetic spectrometer for the detection of light fragments with the needed accuracy, though, would be impractical for a “table top” setup, due to their large angular acceptance. This is the reason why the FOOT apparatus has been designed with two different setups:

- *Electronic Setup*: based on a magnetic spectrometer composed by electronic subdetectors. Optimized for the detection of fragments heavier than He, is able to cover a polar angle of 10° with respect to the beam axis.

- *Emulsion Chamber*: spectrometer based on an emulsion cloud chamber. Will provide measurements of light fragments emitted with angles up to 70°.

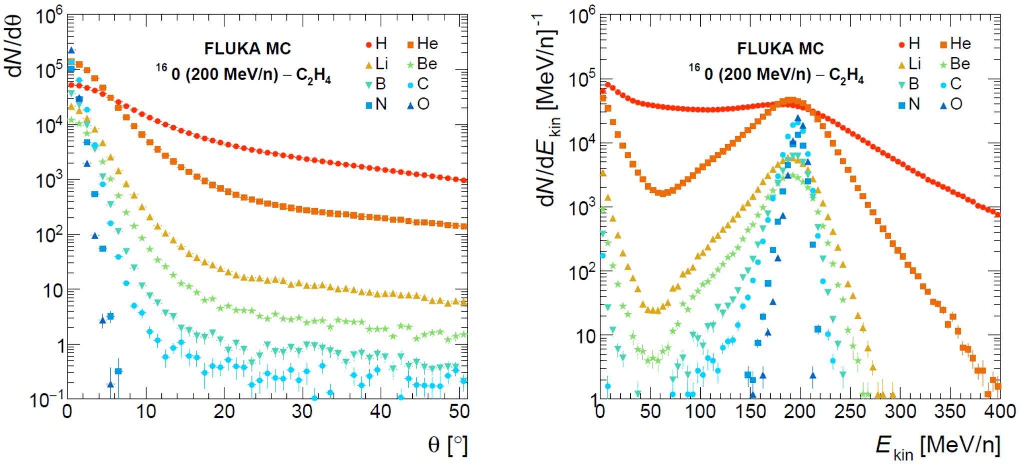

Figure 2.2: MC-computed exit angle (left) and kinetic energy (right) distributions for charged fragments emitted by a 200 MeV/u ^{16}O beam hitting a C_2H_4 target.

2.4 Electronic Setup

The goal of the electronic setup of FOOT is to detect and identify charged nuclear fragments with Z≥3. This is achieved by making use of a magnetic spectrometer, which allows to measure the energy loss (ΔE) of particles, their time of flight (TOF), momentum (p) and kinetic energy (E_k). ΔE and TOF allow to reconstruct the charge, while TOF, p, E_k are employed for the mass reconstruction. In order to obtain the desired precision on the cross section measurement, the needed performances are:

- Momentum resolution $\sigma\left(p\right)/p \sim 5\%$
- Time of flight resolution ~100 ps
- Kinetic Energy resolution $\sigma\left(E_k\right)/E_k \sim 2\%$
- Energy loss resolution $\sigma\left(\Delta E\right)/\Delta E \sim 2\%$

The overall detector size lies between 1.5-2.0 m, which makes it able to exploit therapeutic beams at different centers, such as CNAO (National Center of Oncologic Handrontherapy) in Pavia (Italy), Protontherapy Center in Trento (Italy), HIT (Heidelberg Ion Therapy) Center and GSI Helmholtzzentrum für Schwerionenforschung in Darmstadt (Germany).
The detector can be schematically divided in three different regions: *upstream*

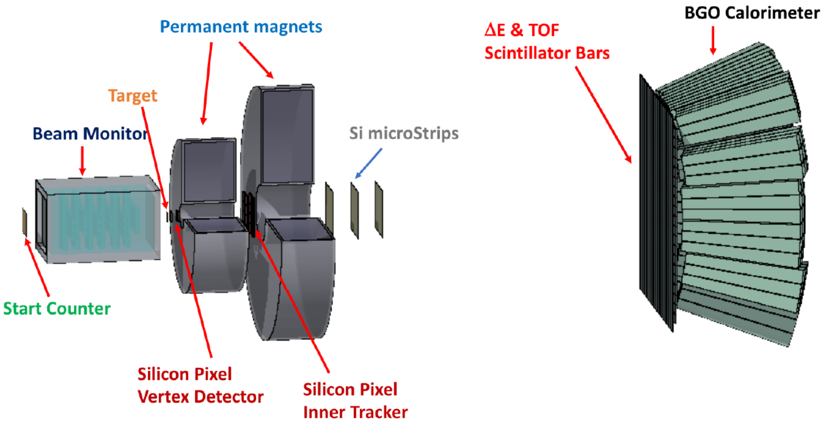

Figure 2.3: Schematic representation of the electronic setup for the FOOT experiment.

region, *magnetic spectrometer* and *downstream* region. The whole layout is depicted in figure 2.3

2.4.1 Upstream Region

This part of the detector is also referred to as *pre-target* region. As a matter of fact, it is composed by two subdetectors that aim at monitoring the direction and interaction point of the beam, as well as at counting the number of primary ions. In this region it is important to minimize the out of target fragmentation and the multiple scattering. The two constituents of the upstream region are the start counter and the beam monitor.

The **Start Counter (SC)** is a squared foil of thin plastic scintillator (EJ-228), with a thickness of 250 μm. The active surface of the scintillator has a transverse size of 5 cm, compatible with the typical transverse beam size. The tightness needed for the detector operation is provided by an aluminium frame enclosed in a 3D printed box, which keeps the scintillator in place. 48 SiPM (AdvanSiD ASD-NUV3S) with a 3x3mm^2 area collect the light. The SiPMs are 12 per side, bundled in 8 channels, each reading a series of 6. The readout and powering of SiPMs is driven by the WaveDAQ system [31], which can sample signals at rates up to 5 Gsamples/s in a dynamic range of 1 V. Since the SC is very thin, a gain between 0.5 and 100 can be applied to its signal and tuned based on beam type and energy. The SC is placed 44 cm upstream of the target. Its jobs are: to provide the trigger, to measure the incoming ion flux and to produce the reference time t_0 for all other subdetectors, allowing the time of flight (TOF) measurement together with

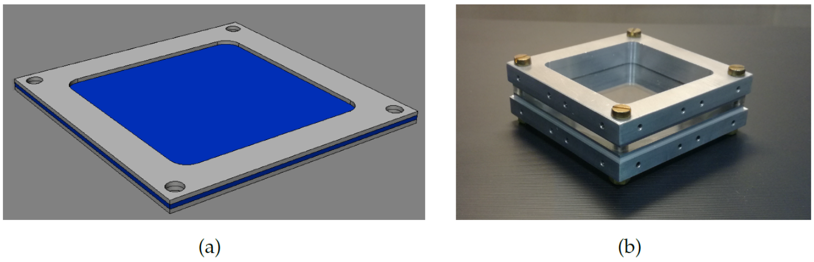
(a) (b)

Figure 2.4: Technical drawing (a) and picture of the mechanical frame (b) of the SC.

the TOF wall detector. Different thicknesses of the scintillator can be used for different projectiles and initial energies to preserve the SC performances. Figure 2.4 shows a technical drawing of the SC and a picture of its frame.

The **Beam Monitor (BM)** is a drift chamber and it has already been used in the FIRST experiment [26]. The chamber consists of 12 layers of wires, with three drift cells per layer. Wires are arranged in planes, alternated along the x and y axes, in order to reconstruct the beam profile. Moreover, consecutive layers are staggered of half a cell, to avoid left-right ambiguities [32]. The cell is rectangular (16x10 mm) and its long side is orthogonal to the beam. The drift chamber operates at a pressure of $\simeq$ 0.9 bar and a working point between 1850 V and 2200 V, depending on the beam. The gas is an Ar/CO_2, 80%/20% mixture. A recent performance study with proton beams [33] has produced some more specific results about the BM. The optimal working point has been found to be ~2200 V and the detection efficiency larger than 90%. The spatial and angular resolutions depend on the initial energy of the beam: the former ranges from 140±70 μm at 220 MeV to 120±60 at 80 MeV, while the latter is respectively equal to 1.62±0.16 mrad and 2.1±0.4 mrad for the same energies. The BM will be placed between the SC and the target, used to measure direction and impinging point of the projectile beam. This information is crucial to address pileup ambiguity in tracking detectors downstream the target. Moreover, it can help discarding events where the beam has fragmented in the SC. A high spatial resolution in the BM is fundamental to measure the direction of emitted fragments with an accuracy of few mrad: this will allow to reach the required resolution for the kinetic energy in inverse kinematic. A schematic view of the BM is presented in figure 2.5, together with a picture showing the inside of the drift chamber.

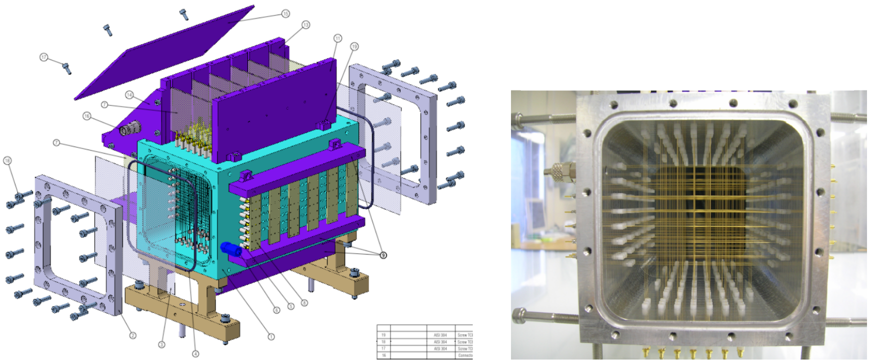

(a) (b)

Figure 2.5: Technical drawing (a) and picture of the inside (b) of the BM.

2.4.2 Magnetic Spectrometer

The central part of the detector includes the target and three tracking stations, all composed by silicon detectors, located upstream, between and downstream of two permanent magnets, which create the magnetic field that curves particles and allows to measure their momentum. The magnetic spectrometer region provides the production point and the tracking of fragments. The **Vertex detector (VTX)** is hosted in a mechanical structure together with the target. It is composed by 4 monolithic pixel sensor layers with an area of 2x2 cm^2. The VTX layers are placed along the z direction, respectively at 0.6-0.9-2.1-2.4 cm from the target: this reflects into a geometric acceptance of $\sim$40° for emitted fragments. MIMOSA-28 (M28) Monolithic Active Pixel Sensor (MAPS) technology has been chosen to build each VTX layer, in order to assure low material budget and high precision and efficiency. The M28 consists in a matrix of 928 (rows) x 960 (columns) pixels with a 20.7 μm pitch, resulting in a chip size of 20.22 x 22.71 mm. Moreover, each M28 layer has a thickness of 50 μm, so that the overall material budget for VTX is 200 μm. To reduce the amount of transferred data, M28 have an integrated binary readout and a zero suppression logic. Moreover, pixels output of one row are read out in parallel row by row at the end of the column, where 960 discriminators are present, each with configurable threshold. The VTX can reach a spatial resolution of 5 μm: matching this value with the BM accuracy, one can reach an angular resolution at the mrad level for the direction of primary beam and emitted fragments. Moreover, the reduced material budget of BM and VTX minimizes multiple scattering. One of the M28 sensors is depicted in figure 2.6. The figure also shows a drawing of one of the VTX layers, with all of its electronics.

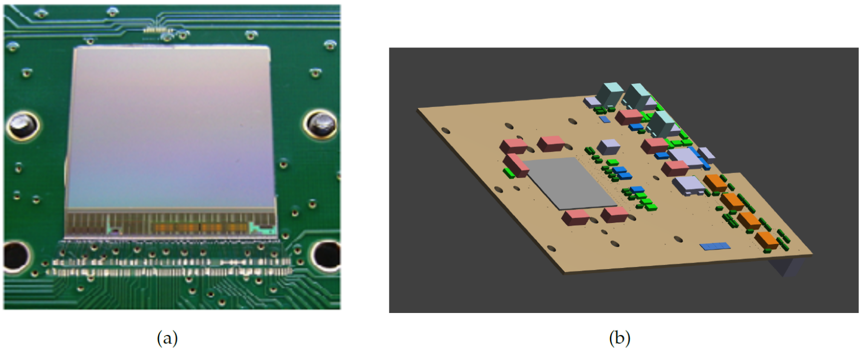
(a) (b)

Figure 2.6: Picture of a M28 sensor (a) and drawing of a VTX layer (b), containing the sensor (gray square) and all the electronics.

The **magnetic system** is a key element of the FOOT spectrometer. It allows to bend the tracks of fragments produced in the target. The ideal choice for this system would be a magnetic dipole, which would be able to guarantee the needed momentum resolution: this choice, though, is not compatible with the requirement of a portable system. The chosen alternative is thus a magnetic system in air, composed by two magnets in Halbach configuration. This allows the presence of a tracking station between the two magnets, to achieve the required momentum resolution. Generally, the Halbach configuration consists in a cylindrical permanent magnet generating an approximately dipolar field in its internal hole. Moreover, the field increases with the radius of the external cylinder and decreases with the radius of the gap. In the case of FOOT, in order to produce the right (B x L) to obtain the wanted momentum resolution and have an angular acceptance of 10°, two different magnet dimensions have been chosen. The first magnet has a gap diameter of 5 cm, the second of 10.6 cm: both generate a field along the y axis, respectively with a maximum intensity of 1.4 T and 0.9 T inside the holes. The intensity of the magnetic field along the z axis of the cylinder exhibits a Gaussian shape for each magnet. The inner tracker, placed in between the two magnets, will experience a magnetic field of 0.6 T. Both magnets are made of twelve units of samarium-cobalt (SmCO), able to maintain its magnetic properties even if exposed to high radiation environments [34].

The **Inner Tracker (ITR)** is a tracking station composed by two layer of pixel sensors, used to track fragments inside the magnetic field region. Each plane covers a sensitive area of $\sim$ 8x8 cm^2, with 16 M28 sensors per layer. This choice is motivated by low material budget, which reduces multiple scattering and out of target fragmentation, and high tracking performances. Moreover, such performances are expected not to significantly change in presence of the magnetic field [35]. The used technology is the same as the VTX, which will simplify the DAQ system, but the larger area with respect to the VTX requires a mechanical support, increasing the material budget. The ITR will consist of *ladders*, i.e. double-sided layouts, similar to the ones already implemented in the PLUME experiment [36]. One of them is shown in figure 2.7. Each ladder will be composed by two modules of M28 sensor layers, glued on opposite sides of a support structure. Each module contains 4 M28 sensors, glued on a cable that provides communication to the outside. The overall material budget of a single ladder is $x/X_0 \simeq 0.3\%$, and the ITR will contain 4 ladders, two for each plane. Figure 2.8 reports a schematic frontal and lateral view of the ITR structure.

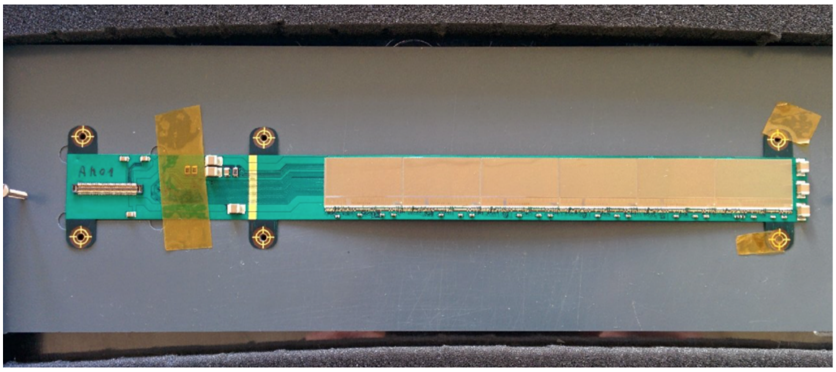

Figure 2.7: Picture of a PLUME ladder [36]. It is a sensor composed by two layers of silicon pixel detectors. In FOOT, it will be used to build the ITR.

The **Micro Strip Detector (MSD)** is the tracking station located downstream of the magnetic region, essential for momentum measurement and matching of reconstructed tracks with hits in subdetectors of the particle-ID region (TOF wall, calorimeter). The MSD operates with an analogue readout, which provides a redundant measurement for the dE/dx of fragments [37], thus for their charge identification. It is composed by three $x-y$ planes with an active area of 9.6x9.3 cm^2, separated by a 2 cm gap along the beam direction. For each $x-y$ plane, the adopted sensors are two perpendicular Single Sided Silicon Detectors (SSSD): this ensures reduced material and $x-y$ readout. Each SSSD has a thickness of 150 μm and is glued to a Printed Circuit Board (PCB) that provides mechanical support and readout interface. A digital readout of the SSSDs with pitch 150 μm would lead

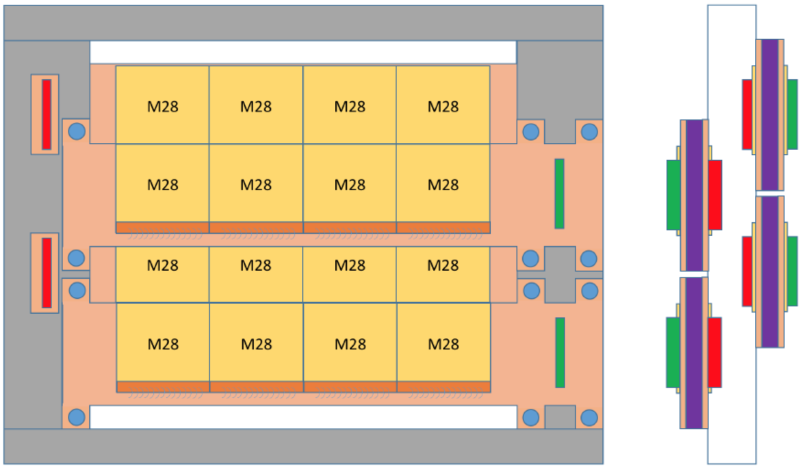

Figure 2.8: Schematic frontal (a) and lateral (b) view of how the ITR will be composed.

to a spatial resolution of about 40 μm, but thanks to the analogue readout a factor 3 can be gained, as proved in [38, 39], with the further advantage of measuring the dE/dx. Analogue signals are read by VA1140 chips, then digitized by 12 bit ADCs.

2.4.3 Downstream Region

The downstream region is also referred to as *fragment identification* region. As a matter of fact, it is composed by two detectors, i.e. the TOF wall and calorimeter, that allow the charge and isotopic identification of fragments. It is the distal part of the detector, located at least 1 m away from the target, but the distance could vary according to the β of the primary beam, to allow an almost constant resolution on the TOF.
The **TOF Wall Detector (TW)** is composed by two layers of 20 plastic scintillator bars (EJ-200, Eljen Technology). Each bar is wrapped with reflective aluminium and darkening black tape. The dimensions of the bars are: 2 cm width, 44 cm length: all of them, arranged on two orthogonal $x-y$ planes, create an active area of 40x40 cm^2. The TW produces the measurement of deposited energy ΔE, the stop signal to the TOF measurement (started with t_0 provided by the SC) and the hit position. The transverse dimensions of the TW have been chosen to match the angular aperture of heavier fragments, dictated by the target-detector distance. Moreover, the thickness of bars is a trade-off between signal intensity, which influences the resolution,

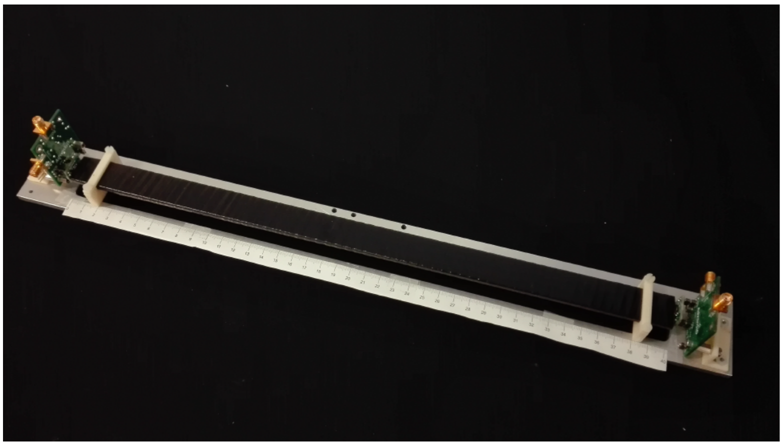

Figure 2.9: Prototype of a plastic scintillator (EJ-200) bar that will be used to build the TW.

and re-fragmentation probability in the TW. Each bar is read by 4 SiPMs, whose signals are digitized by the WaveDAQ system [31], i.e. the same used by the SC. All of the TW characteristics have been chosen to guarantee a time resolution better than 100 ps, a relative energy loss resolution of the order of 5% and a hit position reconstruction with a precision <8 mm. Figure 2.9 shows the prototype of one of the scintillator bars.

The **Calorimeter (CAL)** is the last and most downstream detector, which aims at measuring the kinetic energy of fragments, used to identify their mass A. Since FOOT will work at relatively low beam intensity, the right material for the CAL would be a dense crystal, with high light yield and no particular needs on the response time. For these reasons, bismuth germanate BGO ($Bi_4Ge_3O_{12}$) has been chosen. Its density $\rho = 7.13$ g/cm^3 guarantees a high stopping power and a light yield of $\simeq$10 photons/keV, which meet the energy resolution requirements. The CAL will be composed by 320 BGO crystals in a disk-like arrangement, with an approximate radius of 20 cm. The shape of each crystal will be a truncated pyramid with a front face of 2x2 cm^2, a back face of 3x3 cm^2 and a length of 24 cm. This depth allows to minimize the energy leakage, mostly caused by escaping neutrons. Each crystal is read by a matrix of 25 SiPMs, whose active surface is 2x2 cm^2. The characteristics of the SiPM allow to have a linear response up to an energy of 10 GeV. The SiPM matrix is then coupled to a specific board, which is in turn interfaced with a CAEN V1740 digitizer, that allows measurements based on signal amplitude, signal integral and shape analysis. It is impor-

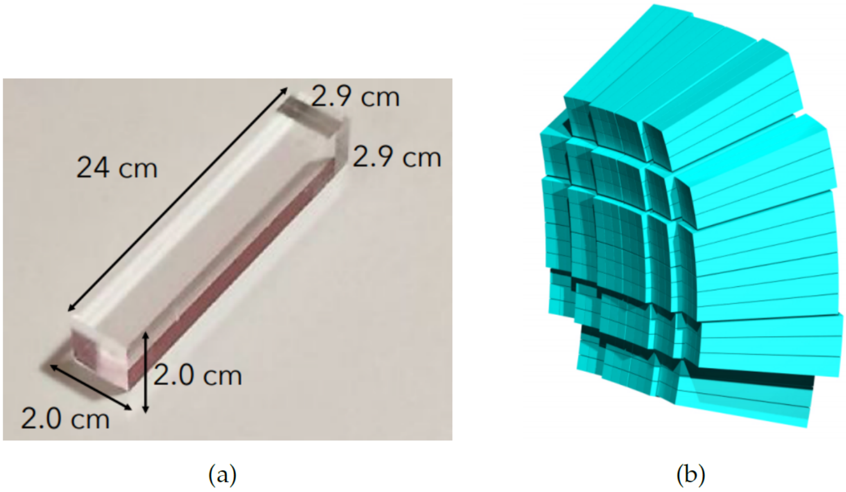

Figure 2.10: Picture of a BGO bar (a) and schematic view (b) of the crystals disk-like disposition for the FOOT calorimeter.

tant to know that, even if the calorimeter fulfills the requirements for kinetic energy resolution as demonstrated from experimental tests [40], E_k can be affected by systematic errors caused by neutron production and, at high energies, hadronic showers that cannot be fully contained. In figure 2.10, the picture of a BGO crystal and the scheme of the disk-like disposition of the calorimeter crystals are shown.

2.5 Trigger and DAQ

The detector will have a DAQ system that has been designed to acquire the largest possible sample size with high accuracy, in a controlled and online-monitored environment. It will have a Minimum Bias Trigger, fired by the SC when its discriminated signal is composed by a number of channels above threshold exceeding a programmable value. In this way, any form of systematics due to trigger selection can be avoided. To improve the fraction of recorded fragmentation events, a fragmentation trigger can be set, asking for activity outside of the central bars of the TW in a logical OR. The electronics used to perform the trigger function is a CAEN V2495 board, with a fully programmable FPGA and internal logic. The maximum acquisition rate in minimum bias trigger will depend on the slowest detectors, i.e. the MIMOSA chips of the pixel tracker. They have a frame readout time of $\sim$185.6 μs, which would imply a maximum readout rate to about 5 kHz, but in order to

reduce the pileup effect in the chips, the actual trigger rate of FOOT will be $\simeq 1$ kHz. With this rate, about 26 M events per day can be collected using a Minimum Bias trigger.
The DAQ system implemented for the whole apparatus is a flexible, hierarchically distributed system based on linux PCs, VME crates and boards, detector integrated readout systems and standard communication links (ethernet, USB, optical fibers). A controller PC will be used for the control of the system: it will run the DAQ GUI interface to start/stop a run, control and configure other nodes in the system. A different PC, called storage PC, will collect information coming from different detectors, perform the event building and store the acquired data on disk. The storage PC will also contain configuration data, DAQ process information and an electronic logbook interfaced with the DAQ system. The whole system is designed to store data on a SSD disk during data taking and transfer data to a dedicated NAS system (>20TB) during inactive times. There will be several sets of online monitoring information. Information pieces on the DAQ running can be collected from each VME board or data provider and provided to a network of PCs connected to the experiment. Moreover, information will also come in the form of histograms filled on each PC: typical histograms will show detector occupancies, particle arrival times, particle energies, collected charges etc. A third, more powerful, online information will come from a fast online event reconstruction performed on the fly for a fraction of events. This will allow to have, on part of the data, track momentum spectra, TOF, fragment charges and masses.

2.6 Emulsion Spectrometer

The Emulsion Spectrometer (ES) has been inserted in the FOOT experiment to work together with the magnetic spectrometer for the characterization of the production of low Z fragments, mostly H and He. The arrangement is shown in figure REF: the ES will be placed after the SC and BM, with the beam incoming from the left. SC and BM, already described in sections REF and REF, will perform their beam monitoring purposes with a DAQ that will be completely decoupled from the one of the ES. SC and BM can be used to perform an online control of the beam flux on the active surface of the emulsions, in order to avoid the spatial pileup of events. The choice of nuclear emulsions for the detection of light fragments has been driven by their excellent spatial resolution ($< \mu$m), which is the best among all tracking devices. In emulsion chambers, target and detector are integrated in a compact setup, providing an accurate reconstruction of interactions occurring inside

the target. A further advantage is that they do not need any power supply or readout electronics. To "read" emulsions, automatic scanning system techniques are needed. Thanks to last generation microscopes, one can have very fast scanning and wide angular acceptance. Summing up, the possibility to measure particles with an angular acceptance above 70° coupled to the very high spatial resolution made nuclear emulsions the ideal choice for the new cross section measurements FOOT wants to perform.
Nuclear emulsion films used by FOOT consist of two 70 μm thick sensitive layers, deposited on both sides of a 210 μm plastic base, producing a total thickness of 350 μm. Sensitive regions are composed by AgBr crystals (2 μm diameter) scattered in a gelatine binder, able to detect charged particles. The trajectory of a charged particle can be recorded by a series of AgBr crystals, which act as latent images. Thanks to the chemical process of development, latent images enhance and induce the growth of silver clusters to a diameter of 0.6 μm, which can be seen with optical microscopes. The density of this cluster, referred to as *grain*, is proportional to the ionization of the charged particle. After the development, emulsions are scanned by automated systems and the acquired image is analyzed by a dedicated software. The goal of this software is to recognize clusters of aligned dark pixels, representing the track of a charged particle: a straight sequence of pixels in an emulsion layer defines a *micro-track*. Then, two aligned micro-tracks on the top and bottom layers of an emulsion form a *base-track*, which can be connected to other base-tracks on a straight line along different films, in order to form a *volume-track*. The FOOT emulsion spectrometer has been built with alternated layers of passive materials and nuclear emulsions, acting as high-resolution tracking detectors and ionization detectors. Also in this case, the setup can be ideally divided into three sections with different purposes.

- *Interaction and Vertexing Region*: this first section is composed by layers of target element, in this case C or C_2H_4, alternated with emulsion films. When the primary beam interacts with the target cells of this sections, secondary fragments will be emitted and detected by the following sections. Thanks to the emulsion structure, the detector will track the fragments and reconstruct the interaction position. The length of the first section has to be optimized for each data taking, in order to have a statistically significant number of interactions based on the beam type and energy and on the target. During the 2019 data taking at GSI, two ^{12}O beam configurations, at 200 MeV/u and 400 MeV/u have been detected with two different stacks of 30 cells. In the former case the target was composed by 1 mm carbon layers, while in the latter 2 mm C_2H_4 layers were used.

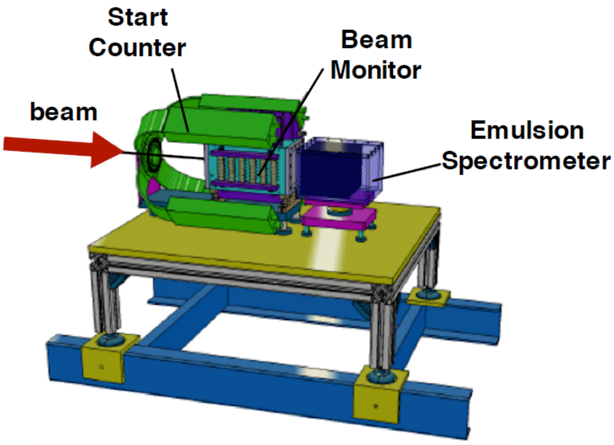

Figure 2.11: Layout of SC and BM placed next to the emulsion spectrometer to monitor the beam before the interaction.

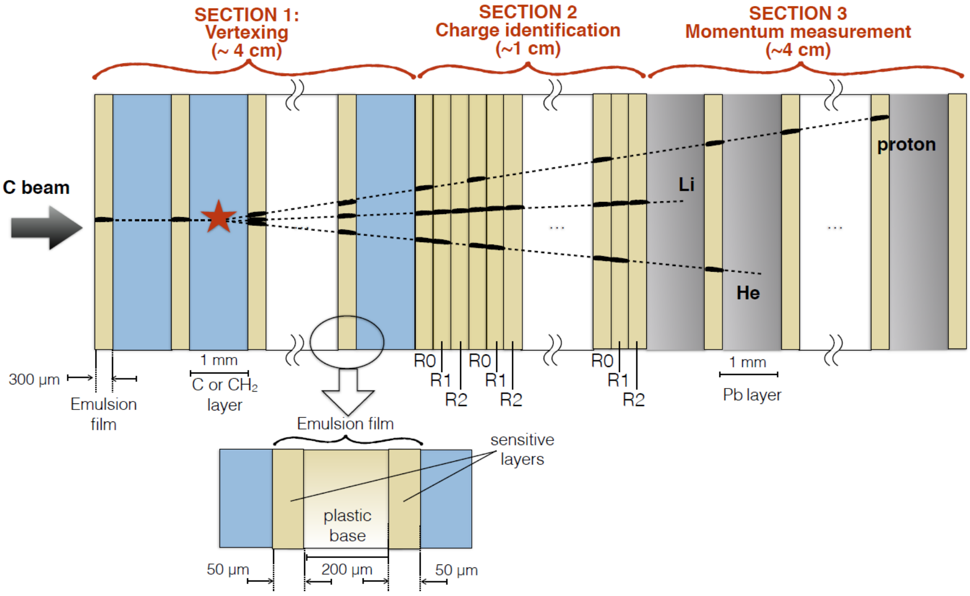

Figure 2.12: Schematic description of the emulsion spectrometer and the materials composing it, divided in three sections.

- *Charge Identification Region*: composed by elementary cells consisting of four emulsion films, without any passive material. The section is dedicated to Z identification, which can be achieved by measuring the grain density, proportional to the energy loss. In exposing the emulsions to charged particles, one has to take into account that highly ionizing particles can cause a saturation effect, suppressing the identification possibility. However, by thermally treating the emulsions at an appropriate temperature above 28°C and at high humidity ($\sim 95\%$) for about 24 hours, one can induce a fading that can reduce the number of tracks. The combination of several films, subject to different temperatures, allows to overcome saturation effects for particles with different ionizations [41, 42]. This procedure, called *refreshing*, has to be performed after the exposure and before the chemical development. In the case of FOOT emulsions, refreshing has been applied with different temperatures, each producing different track volume variables for the particles, proportional to the silver grain density [43]. The charge of fragments can be identified by looking at the correlation between couples or linear combination of volume track variables.

- *Momentum Measurement Region*: composed by emulsion slabs alternated with passive material. The dimensions of section 3, i.e. length, number of layers and thicknesses, depend on the beam energy. The accuracy of the reconstruction depends on the segmentation of high-Z passive layers, which has to be chosen in order to stop the fragments. In the stack, passive layers with lower Z are placed before the ones with high Z. The kinetic energy is evaluated with the range technique: measuring the length of the track, E_k can be estimated using the range-momentum energy correlation. The momentum of particles can be estimated, using the trajectory, through the Multiple Coulomb Scattering Method (MCS) [44, 45]. By measuring with high accuracy the $x - y$ coordinates and their slopes (θ_x, θ_y) for each track, the MCS method allows to estimate the momentum as:

$$p\,(MeV/c) = \frac{13.6}{\beta \cdot \delta\theta\,(mrad)} \cdot Z \cdot \sqrt{\frac{x}{X_0}} \tag{2.11}$$

  where β is the velocity of the fragment, Z its charge, $\delta\theta$ the deviation of the track slope, x the traversed distance and X_0 the radiation length in the material. The use of two independent methods for energy and momentum estimation, together with the charge measurement of the previous section, allows the assessment of the mass A for the isotopic identification.

Chapter 3

Global Analysis and Lagrange Multipliers Method

The fragment reconstruction procedure of the FOOT experiment allows to identify nuclear fragments by spotting their charge Z and mass number A. In this thesis, the reconstruction relies on Monte Carlo (MC) simulated data obtained with the FLUKA software. This chapter will contain, in section 3.1, an overview of the simulation that produced data used for the analysis; in section 3.2 an outline of the charge and mass reconstruction performances, together with their physical basis, will be presented. Section 3.3 will then describe the theory at the basis of the Lagrange Multipliers method, together with its application to fragments identification in the framework of the FOOT analysis code. In section 3.4 the results of mass number reconstruction using the Lagrange Multipliers method will be presented.

3.1 Monte Carlo simulations

The complete simulation of the FOOT setup has been a very important tool during the planning stage of the apparatus: it has been performed for different ion beams, initial kinetic energies and targets. In this way, the geometry and performances have been corrected and optimized by accurately evaluating the interactions in the active parts of the detector and identifying possible critical points in the layout. The software implied for all simulations is FLUKA [28, 29], which was chosen thanks to its robustness, coming from the comparison with many experimental data, and because it is now widely implied in several fields of physics. The code is able to simulate the interaction and transport of hadrons, heavy ions and electromagnetic particles [46]. To simulate the interaction of such particles with different materials, FLUKA

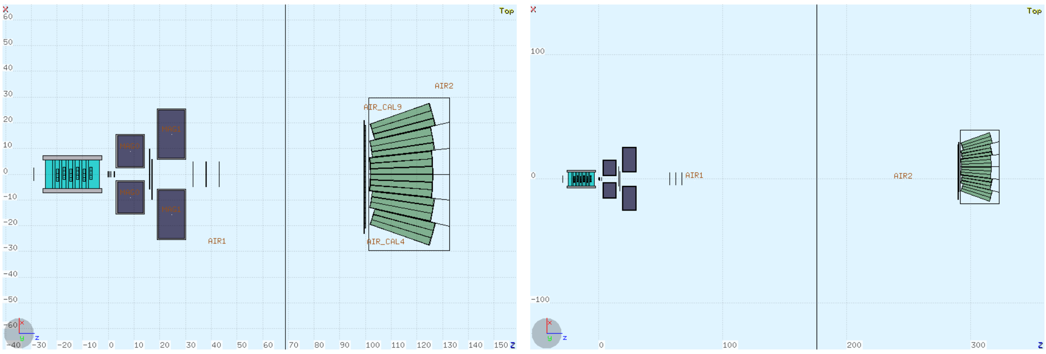

(a) 200 MeV/u

(b) 700 MeV/u

Figure 3.1: Simulated layout of the FOOT detector, for two different initial energies of the primary beam. This 2D view has been created with FLUKA Flair GeoViewer [47].

makes use of experimental cross sections if available, or different theoretical models according to the particle type and energy.

The simulation used in this thesis to perform the analysis is based on the geometry of the electronic setup described in section 2.4. In this geometry, the origin of the reference frame is placed at the center of the target, with all the subdetectors placed along the z axis, which also coincides with the beam direction. At present, the primaries are simulated as a beam along the z direction, with a small spread in the transverse directions, mimicking a real therapeutic beam. Experts decided not to include in the simulation step any detectors response efficiency or smearing, as they will be implemented in the reconstruction step. This chapter contains an analysis of the fragmentation of two primary beams of ^{16}O, respectively with initial energies of 200 MeV/u and 700 MeV/u. The former value provides results that are compatible with the hadrontherapy energy range, while the latter can give information for space radiation protection.

The geometries for both layouts are respectively reported in figures 3.1(a) and 3.1(b). In both cases, the beam impinges on a polyethylene (C_2H_4) target with a density $\rho = 0.94\ g/cm^2$ and a thickness of 5 mm: this target produces a nuclear fragmentation rate of 2.8% and 1.2%, respectively, for 200 and 700 MeV/u beam energies. When the initial energy of the beam is higher, i.e. at 700 MeV/u, a different setup has been used: due to the lower emission angle of the produced fragments, the detectors have been placed further away from the target, in order to have the same angular acceptance. In particular, the MSD is placed 62 cm away from the target and its planes are spaced of 5 cm, then, TOF wall and calorimeter are placed at 290 cm from the target and the

Beam Energy	Primary Particles	Interaction Events
200 MeV/u	$5 \cdot 10^7$	1397243
700 MeV/u	$1 \cdot 10^7$	121118

Table 3.1: Number of primary particles and interaction events simulated with FLUKA for two different initial energies of the primary ^{16}O beam impinging oh a 5mm C_2H_4 target, studied in the present work.

calorimeter is slightly moved in the x direction to account for magnetic deflection. Table 3.1 reports the values of primary particles and selected events for each initial energy of the beam.

To obtain a more acceptable computing time and output data size, simulation experts decided to set a transport threshold of 1 GeV for produced photons, electrons, γ-rays and e^+e^- pairs, so that they deposit all of their energy in the same point where they are produced. Moreover, photons transport was allowed in the whole simulated apparatus because it does not affect computing resources, while e^+e^- pairs transport was switched off in the magnetic field and calorimeter area to speed up the process and avoid very large sizes for output files.

3.2 Fragments Identification

The MC simulation produced by FLUKA allows to reconstruct the trajectory produced by a fragment as a series of hits along the detector volume. Once all the hits of a given fragment have been collected, the analysis code converts trajectories into track objects, which are represented by a C++ *struct*. The whole code, composed by C++ classes and ROOT, will then work with these objects. When all the tracks have been inserted into the analysis code, the first step is to identify the charged fragment that produced them: a nuclear fragment is uniquely identified by the value of its charge Z and mass number A. The FOOT apparatus allows to obtain the values of Z and A by measuring the energy release in a thin scintillator (i.e., the TW), their time of flight, momentum and kinetic energy. The time of flight is measured between the SC and TW, the kinetic energy is measured as the energy deposited in the CAL and the momentum is reconstructed by the magnet bending in the tracking region. This implies that all fragments included in the analysis have to traverse the whole detector, from SC to CAL, in order to be correctly identified. All kinematic quantities used for the identification have some specific features, which will be presented in the following.

The energy loss (ΔE) of particles is reconstructed as the energy released in the plastic scintillator. Experimental tests allowed to parametrize the resolution of ΔE as a function of the energy loss itself:

$$\sigma\left(\Delta E\right) = \alpha + \frac{\beta}{\Delta E} \tag{3.1}$$

where α=0.904 MeV and β=18.6 MeV^2. It is worth to notice that ΔE is also proportional to the charge Z of the fragment (see eq. (1.1)). The energy loss resolution can then be identified with the resolution of the scintillator, which has been experimentally proven to be limited in the range [5; 10]%.

$$\frac{\sigma\left(\Delta E\right)}{\Delta E} = \frac{\sigma\left(\Delta E_{scn}\right)}{\Delta E_{scn}} \tag{3.2}$$

The time of flight (TOF) is reconstructed as the time window between a signal in the SC detector and a signal in the TW, placed in the downstream region. Both signals are produced in thin layers of material and collected by silicon photomultipliers to minimize the delay between signal production and acquisition. The TOF resolution is a function of both the initial energy of the beam and the energy released in the TW, which depends on its charge. These dependencies have been experimentally investigated: the TOF resolution as a function of the initial kinetic energy has been proven to range from 54 to 84 ps, as shown in plot 3.2(a). The proportionality with the charge of the fragment, instead, is reported in plot 3.2(b) and it is a function of $1/Z$. Taking into account these two dependencies, σ(TOF) can be empirically parametrized as:

$$\sigma_{TOF} = A + \frac{B}{Z} \tag{3.3}$$

where A = 56 and B = 84. According to the formula (3.3), the resolution is approximately 70 ps for carbon ions and 140 ps for hydrogen. Further and more specific details on the evaluation of TOF resolution can be found in [48].

The resolution σ(TOF) is taken into account in the analysis code by applying a Gaussian smearing to the TOF value produced by the simulation: the smearing is calculated by means of equation (3.3). Adding the measurement of the distance L travelled by the particle, which can be obtained by the tracking from the production point to the entrance of the TW, the TOF measurement can also be used to calculate the velocity β of the fragment in units of c as:

$$\beta c = \frac{L}{TOF} \tag{3.4}$$

The momentum (p) of fragments can be extracted from the angular deviation of the track inside the magnetic field of the spectrometer. Its resolution

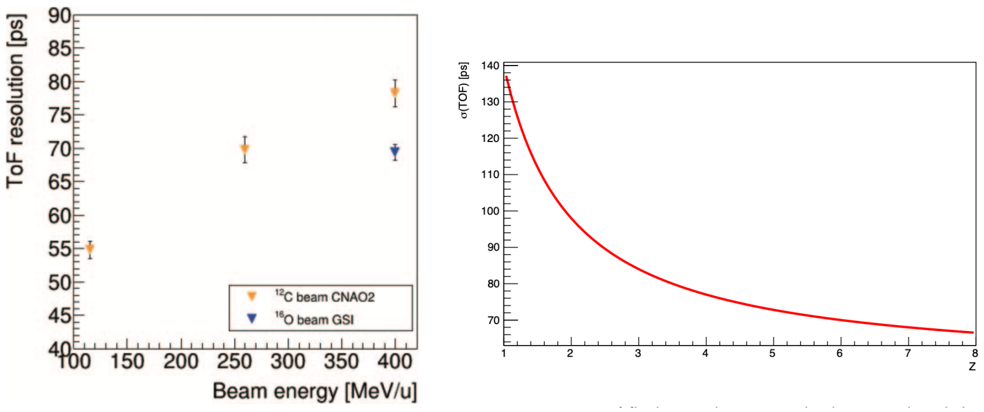

(a) TOF resolution as a function of initial kinetic energy of the beam [48]

(b) TOF resolution as a function of charge

Figure 3.2: TOF resolution as a function of the two variables used to parametrize it in equation (3.3): beam energy and charge of the fragment.

contains several contributions, namely the spatial resolution of detectors, the spatial extension and intensity of the magnetic field and the multiple Coulomb scattering, which is inversely proportional to the energy and mass of particles. Experimental studies used Kalman Filter tool [49], which is the main technique involved in track reconstruction to evaluate the momentum, to prove that the resolution improves with energy and, subsequently, with the momentum of fragments. This is due to the reduced multiple scattering contribution, but also depends on the spatial resolution of trackers, which ranges from few μm to tens of μm. Nevertheless, the difference between the resolution of light and heavy fragments is negligible, and has been considered constant for the analysis presented in this chapter. Using the MC generated and reconstructed momenta, p_{gen} and p_{reco}, the relative momentum resolution can be derived as:

$$\frac{\sigma(p)}{p} = \frac{p_{gen} - p_{reco}}{p_{reco}} \tag{3.5}$$

Momentum resolution resulted about $\sigma_p/p = 3.7\%$ as a good approximation for all fragments produced by beams with initial energies of 200 MeV/u and 700 MeV/u. This implies that the reconstructed momentum can be obtained by applying a Gaussian smearing of 3.7% to the value p_{gen} produced by the FLUKA code.

The kinetic energy (E_k) of fragments can be estimated as the value of energy deposited by particles inside the calorimeter. This value is obtained by summing the energy deposition of a given fragment in each crystal composing the

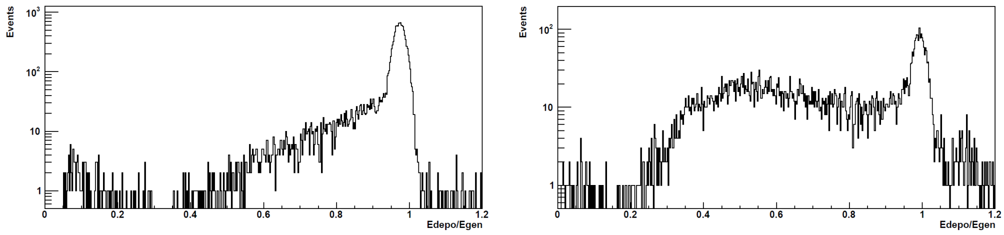

(a) 200 MeV/u

(b) 700 MeV/u

Figure 3.3: Ratio of deposited energy and MC generated energy for ^{12}C produced by a 200 MeV/u and a 700 MeV/u beam of ^{16}O impinging on a C_2H_4 target.

calorimeter, in order to include also the re-fragmentation contributions. The main drawback in the measurement of E_k is the production of neutrons in elastic interactions with atoms of the calorimeter: neutrons can deposit their energy far from the primary track or, sometimes, out of the detector, leading to a constant underestimation of the fragment energy. To have a slightly more precise evaluation of the kinetic energy of the fragments, the energy loss contributions of TW and MSD have been included. Figure 3.3 reports the ratio of energy deposited in calorimeter and scintillator with respect to the MC generated energy. Defining as good reconstructed fragments the ones that deposit in CAL an energy that differs less than 10% from their generated one, we can see that an amount of 17% and 75% of fragments, respectively for 200 and 700 MeV/u, are not well reconstructed. This effect is due to the larger neutron production and the larger fraction of energy deposited in other subdetectors, which cannot be measured.

The resolution of kinetic energy measured in a calorimeter is usually expressed as:

$$\frac{\sigma\left(E_k\right)}{E_k} = \frac{c_1}{\sqrt{E_k}} + \frac{c_2}{E_k} + c_3 \tag{3.6}$$

and, in the specific case of the FOOT calorimeter, we have: $c_1 = 1.84$ MeV$^{1/2}$, $c_2 = 96.16$ MeV, $c_3 = 0.37$. From experimental tests with different types of beams at several initial energies, it has been found that the resolution is dominated by the constant term c_3, which is mainly due to inhomogeneities of the calorimeter and shower leakage. The estimation of relative resolution $\sigma\left(E_k\right)/E_k$ lead to a constant value of 1.5%, which has been applied as a Gaussian smearing to all MC values of kinetic energy in the analysis.

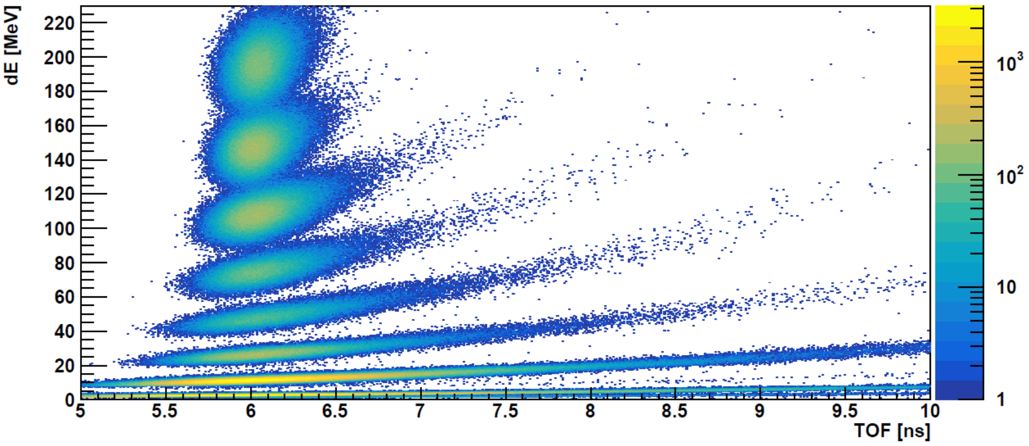

Figure 3.4: Time of Flight vs energy loss in the TW for fragments produced by a 200 MeV/u beam of ^{16}O on a polyethylene target. In the plane, eight regions are visible, which represent fragments with charges from 1 to 8.

3.2.1 Charge Identification

The charge Z of fragments can be calculated by inverting the Bethe Bloch equation (1.1): in the analysis, the quantity dE/dx of the formula becomes the energy deposit ΔE in the TW, while the velocity β is determined according to equation (3.4). The TOF-ΔE plot obtained in my analysis and reported in figure 3.4 for a beam with initial energy = 200 MeV/u shows that the resolutions of energy loss and time of flight allow to discriminate eight regions in the plane, which correspond to fragments with charge from 1 to 8. The eight regions are distributed on the $TOF - \Delta E$ plane according to the Bethe-Bloch curve for the corresponding charge.

Figures 3.5(a) and 3.5(b) report the results I obtained for the charge identification of fragments produced by a beam of ^{16}O hitting a polyethylene target at, respectively, 200 MeV/u and 700 MeV/u. From the plots it is evident that, despite some small tails, the features of the FOOT apparatus allow a good charge separation and the identification capability depends mainly on the ΔE resolution. Plots 3.5(a) and 3.5(b) both show a small peak before the proper hydrogen peak: its cause has not been understood yet and is still under investigation. My results of mean values and resolutions for the charge identification at initial beam energies of 200 and 700 MeV/u are summed up in table 3.2. In the case of an oxygen beam with initial energy of 200 MeV/u, the charge resolution has its best value of about 3% for heavy fragments, while it reaches almost 6% for hydrogen.

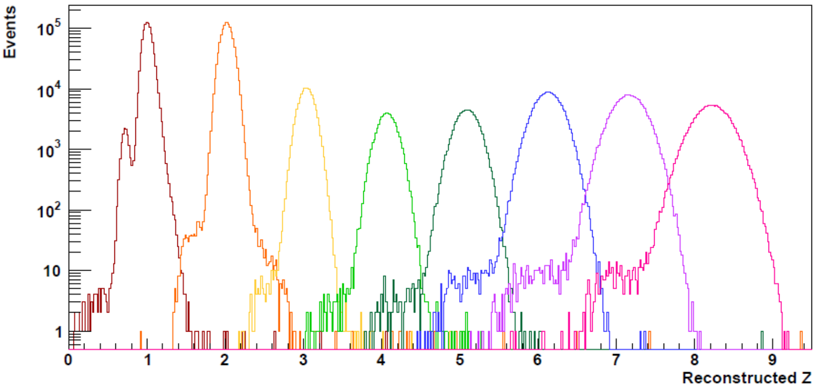

(a) 200 MeV/u ^{16}O on C_2H_4

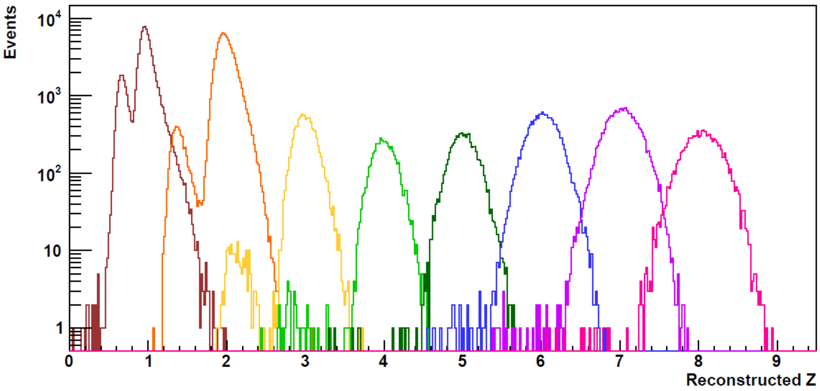

(b) 700 MeV/u ^{16}O on C_2H_4

Figure 3.5: Reconstructed charges for fragments produced by a beam of ^{16}O at, respectively, 200 and 700 MeV/u hitting a polyethylene target.

	200 MeV/u		700 MeV/u	
Fragment	**Z**	σ_Z [%]	**Z**	σ_Z [%]
H	1.01	5.5	0.96	6.2
He	2.02	3.6	1.97	4.9
Li	3.04	3.2	2.99	4.4
Be	4.07	3.0	3.99	3.6
B	5.09	2.9	5.01	3.2
C	6.13	2.8	6.02	3.2
N	7.16	2.8	7.03	3.0
O	8.20	2.8	8.05	2.9

Table 3.2: Reconstructed charge and charge resolution for fragments produced by a ^{16}O beam impinging on a C_2H_4 target with, respectively, 200 MeV/u and 700 MeV/u.

Resolutions are slightly worse for a beam with 700 MeV/u, where σ_Z reaches a value of 6.2%. It is worth to remind, though, that light fragments (H, He) will also be identified using data from the emulsion spectrometer, thus it is acceptable for these charges to have less precise results. Anyway, at both energies the peaks are very well resolved and the probability to not identify the correct charge is at percent value.

3.2.2 Mass Identification

The second step of fragments identification is the evaluation of its number of mass A which, combined with Z, allows to uniquely identify the particle. The most important feature of the FOOT apparatus is the redundancy of the subdetectors, which enables to determine A, thus make an isotopic identification, in three different ways. A_1, A_2 and A_3 are obtained by the combination of two of the three kinematic quantities of the fragment: time of flight (TOF), momentum (p) and kinetic energy (E_k).

- *A1: combination of TOF and p*
  Relativistic particles obey to an equation that relates their mass m with their momentum p and velocity β:

  $$p = mc\beta\gamma \tag{3.7}$$

  Inverting equation (3.7) and reminding that $A = m/U$, where U is the atomic mass unit, U = 931.494 MeV/c^2, we obtain:

  $$A_1 = \frac{p}{U\beta c\gamma} \tag{3.8}$$

where

$$\gamma = \frac{1}{\sqrt{1-\beta^2}} \tag{3.9}$$

Moreover, using error propagation, we can estimate the resolution:

$$\begin{aligned}\sigma\left(A_1\right) &= \sqrt{\left(\frac{\partial A_1}{\partial p}\sigma\left(p\right)\right)^2 + \left(\frac{\partial A_1}{\partial \beta}\frac{\partial \beta}{\partial TOF}\sigma\left(TOF\right)\right)^2} \\ &= \frac{1}{U}\frac{p}{\beta c}\sqrt{\frac{1}{\gamma^2}\left(\frac{\sigma\left(p\right)}{p}\right)^2 + \frac{\gamma^2}{\beta^2}\frac{L^2}{c^2\,TOF^2}\sigma^2\left(TOF\right)}\end{aligned} \tag{3.10}$$

- *A_2: combination of E_k and TOF*
  A relativistic equation involving the kinetic energy and the mass of the fragment is considered:

$$E_k = mc^2\left(\gamma - 1\right) \tag{3.11}$$

Then, inverting the equation (3.11) and considering the expression for A written above, we obtain:

$$A_2 = \frac{E_k}{U \cdot c^2\left(\gamma - 1\right)} \tag{3.12}$$

In this case, the associated resolution is:

$$\begin{aligned}\sigma\left(A_2\right) &= \sqrt{\left(\frac{\partial A_2}{\partial E_k}\sigma\left(E_k\right)\right)^2 + \left(\frac{\partial A_2}{\partial \beta}\frac{\partial \beta}{\partial TOF}\sigma\left(TOF\right)\right)^2} \\ &= \frac{E_k}{U\beta c}\frac{\gamma}{\gamma - 1}\sqrt{\frac{1}{\gamma^2}\left(\frac{\sigma\left(E_k\right)}{E_k}\right)^2 + \frac{\beta^2\gamma^4}{\left(\gamma-1\right)^2}\frac{L^2}{c^2\,TOF^2}\sigma^2\left(TOF\right)}\end{aligned} \tag{3.13}$$

- *A_3: combination of E_k and p*
  To obtain the third expression of the mass number, two relativistic expressions for the energy of the particle must be taken into account:

$$E = E_k + mc^2 \tag{3.14}$$

$$E = \sqrt{p^2c^2 + m^2c^4} \tag{3.15}$$

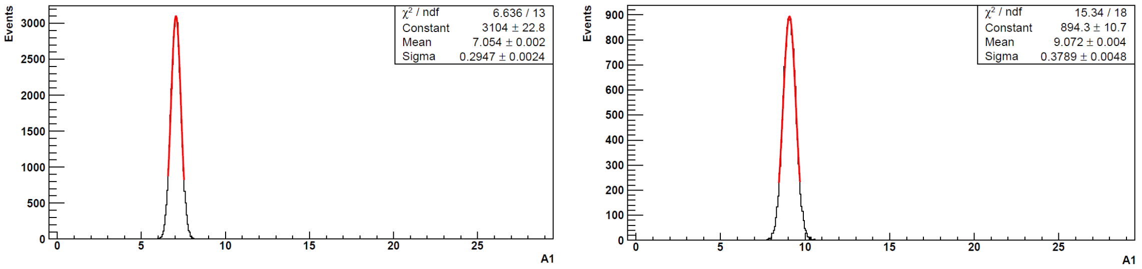

(a) ^{7}Li (b) ^{9}Be

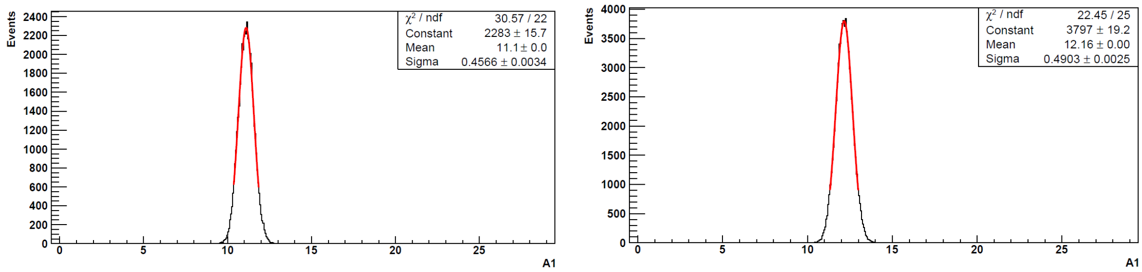

(c) ^{11}B (d) ^{12}C

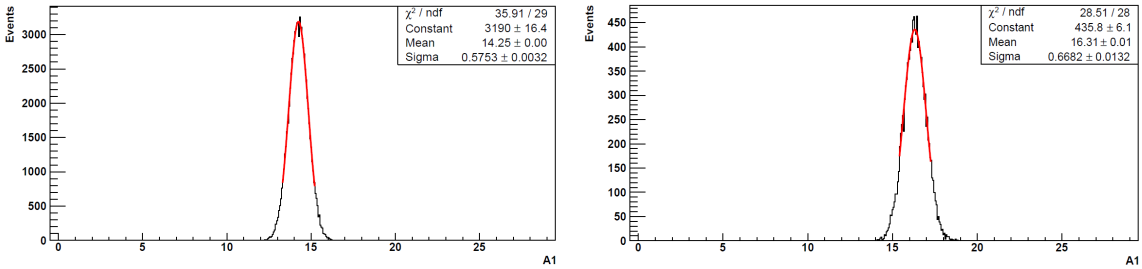

(e) ^{14}N (f) ^{16}O

Figure 3.6: Distribution of reconstructed mass number A_1 obtained with equation (3.8) for the most abundant isotope of each charge $Z \geq 3$ for initial energy 200 MeV/u.

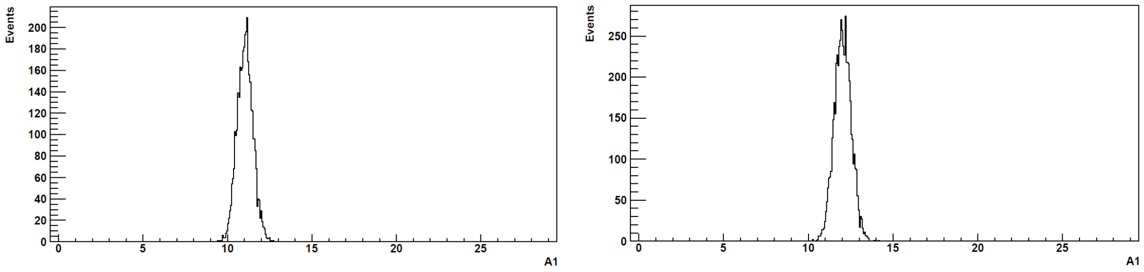

(a) ^{11}B (b) ^{12}C

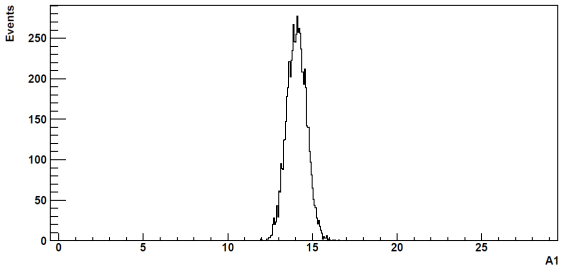

(c) ^{14}N

Figure 3.7: Distribution of reconstructed mass number A_1 obtained with equation (3.8) for some of the most abundant isotopes for initial energy 700 MeV/u.

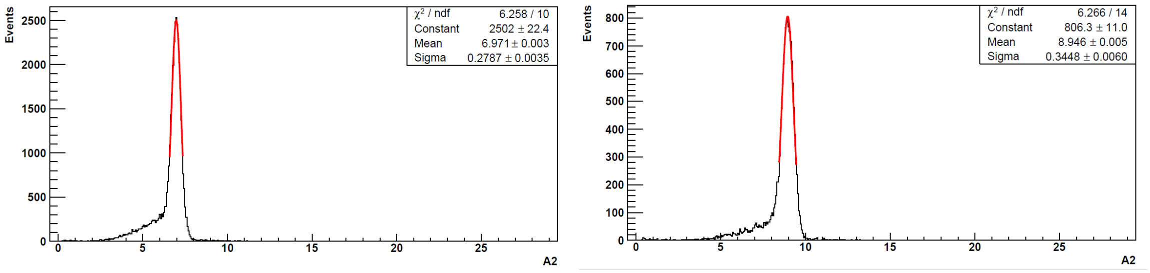

(a) ^{7}Li (b) ^{9}Be

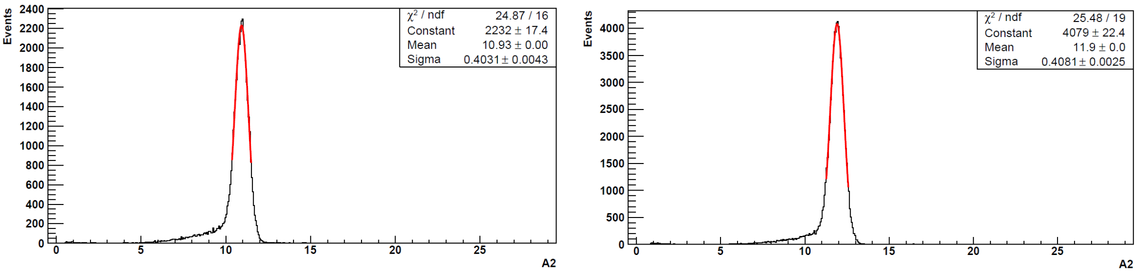

(c) ^{11}B (d) ^{12}C

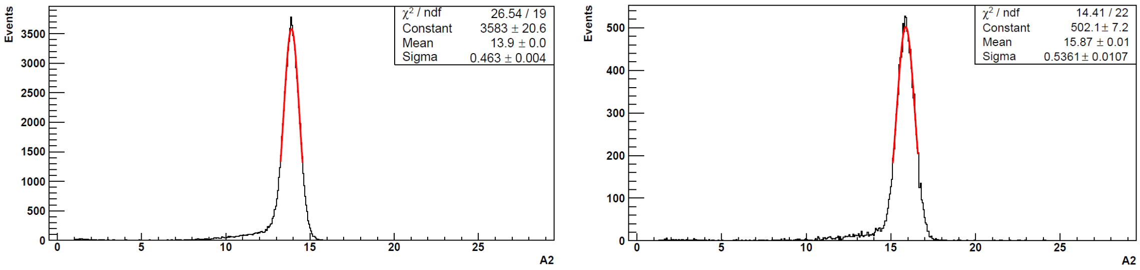

(e) ^{14}N (f) ^{16}O

Figure 3.8: Distribution of reconstructed mass number A_2 obtained with equation (3.12) for the most abundant isotope of each charge $Z \geq 3$ for initial energy 200 MeV/u.

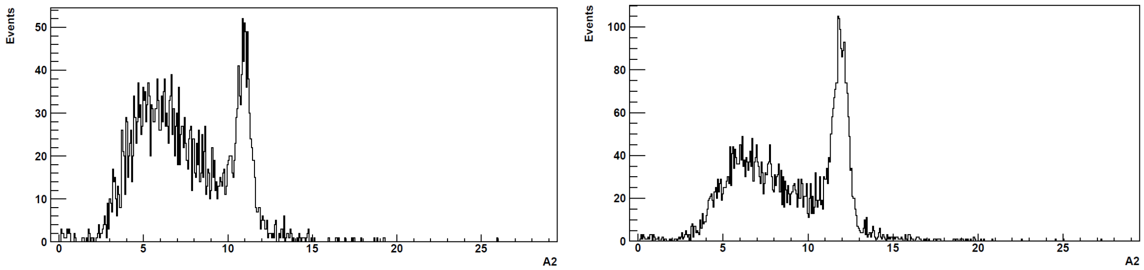

(a) ^{11}B (b) ^{12}C

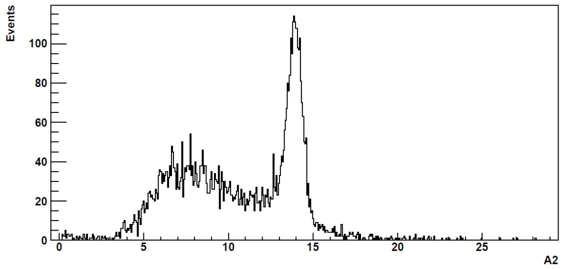

(c) ^{14}N

Figure 3.9: Distribution of reconstructed mass number A_2 obtained with equation (3.12) for some of the most abundant isotopes for initial energy 700 MeV/u.

By combining (3.14) and (3.15), it is possible to calculate the mass m of the fragment, which can then be divided by U to retrieve the mass number A$_3$:

$$m = \frac{p^2c^2 - E_k^2}{2c^2E_k} \tag{3.16}$$

$$A_3 = \frac{p^2c^2 - E_k^2}{2Uc^2E_k} \tag{3.17}$$

Then, the associated resolution can be evaluated as:

$$\begin{aligned}\sigma\left(A_3\right) &= \sqrt{\left(\frac{\partial A_3}{\partial p}\sigma\left(p\right)\right)^2 + \left(\frac{\partial A_3}{\partial E_k}\sigma\left(E_k\right)\right)^2} \\ &= \frac{1}{UE_k}\sqrt{p^4\left(\frac{\sigma\left(p\right)}{p}\right)^2 + \frac{p^2c^2 + E_k^2}{4c^4}\left(\frac{\sigma\left(E_k\right)}{E_k}\right)^2}\end{aligned} \tag{3.18}$$

The distributions of A$_1$, A$_2$ and A$_3$ obtained in my analysis for some selected fragments produced by a beam of ^{16}O hitting a polyethylene target are shown in figures 3.6, 3.8, 3.10 for a beam energy of 200 MeV/u and in figures 3.7, 3.9, 3.11 for a beam energy of 700 MeV/u. All distributions contain a peak, whose mean value is compatible with the expected mass number of the fragments: every difference from the true value is indeed included in the resolution. Moreover, the width of each distribution depends on the resolution or, equivalently, the smearing applied to the kinematic quantities involved in the A calculation. The mass number resolution is about 4% for A$_1$, slightly better for A$_2$, where it reaches a value of 3.2% for heavier fragments, and worse for A$_3$, for which σ_A is of the order of 8-9%. The worse precision of A$_3$ with respect to A$_1$ and A$_2$ is explained in equation (3.17), where the momentum and kinetic energy are squared and, subsequently, the associated error is multiplied by a factor 2. A common feature of all plots showing the distributions of A$_2$ and A$_3$ is a tail before and after the peak: this tail is due to the kinetic energy underestimation caused by the neutron production in the calorimeter, leading to an underestimation/overestimation of the mass number. In this analysis, though, the contributions of energy loss in the TW and MSD have been included in the kinetic energy, in order to have a slightly more precise estimation of A.

It is important to underline that equations (3.8), (3.12) and (3.17) are not independent from each other: the three mass number determinations are correlated, due to the presence of a common subdetector for each couple of equations. Therefore, it is necessary to apply a fit procedure that includes

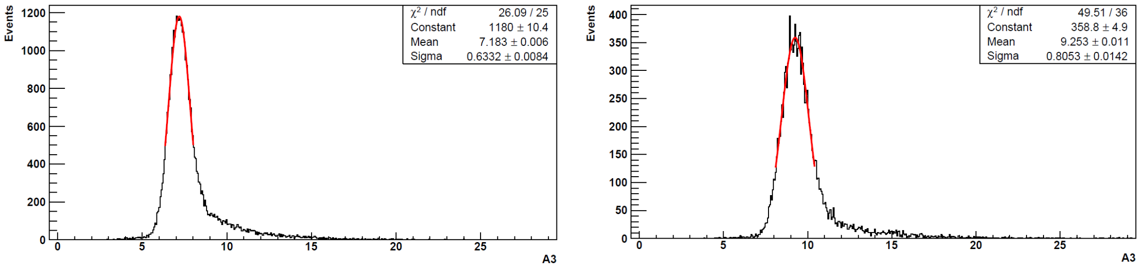

(a) ^{7}Li (b) ^{9}Be

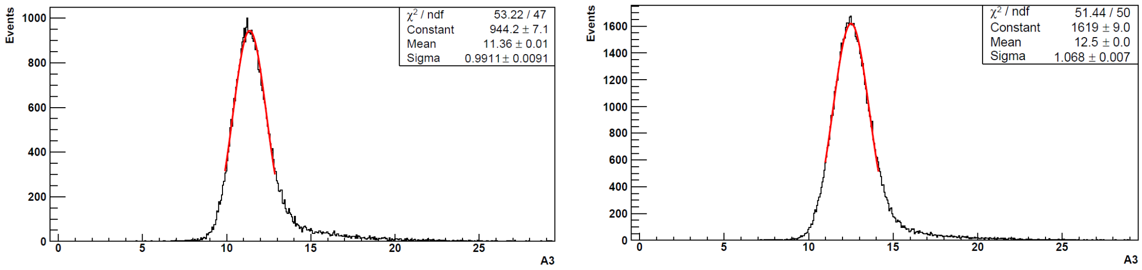

(c) ^{11}B (d) ^{12}C

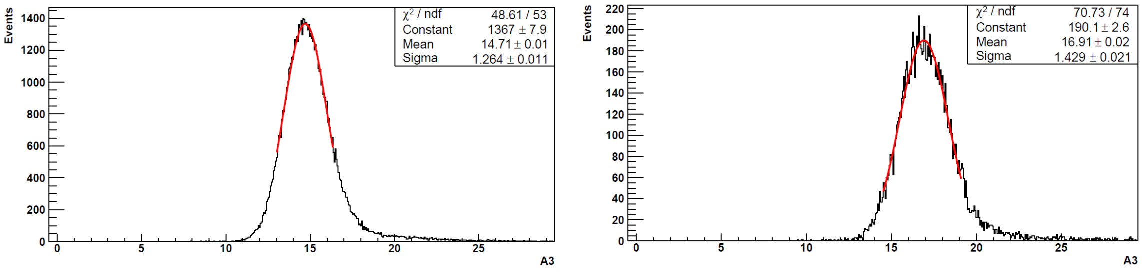

(e) ^{14}N (f) ^{16}O

Figure 3.10: Distribution of reconstructed mass number A_3 obtained with equation (3.17) for the most abundant isotope of each charge $Z \geq 3$ for initial energy 200 MeV/u.

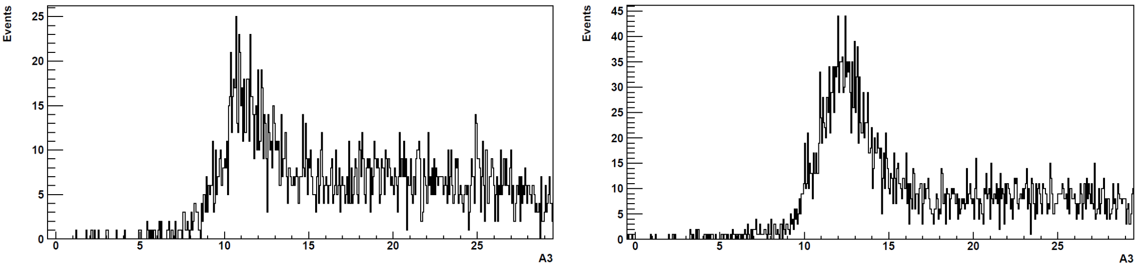

(a) ^{11}B

(b) ^{12}C

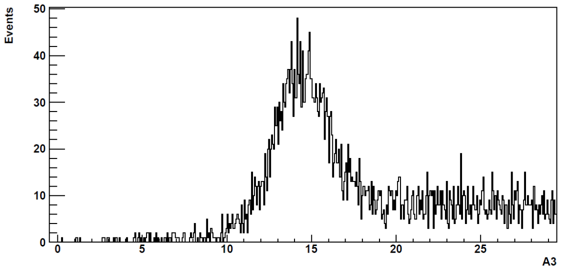

(c) ^{14}N

Figure 3.11: Distribution of reconstructed mass number A_3 obtained with equation (3.17) for some of the most abundant isotopes for initial energy 700 MeV/u.

A_1, A_2 and A_3 simultaneously and allows to obtain the best estimation for A. In the analysis code of FOOT experiment, two fit procedures have already been implemented, one based on the χ^2 minimization [50] and another on the Augmented Lagrangian Method (ALM) [51]. The main work of this thesis is to implement a third fit procedure for A, based on the Lagrange Multipliers method. In the following, a theoretical description of this technique will be presented, together with the implementation of the method in the FOOT analysis code and the results obtained for the number of mass estimation.

3.3 Lagrange Multipliers Method

The method of Lagrange Multipliers (LM) is a tool for constrained minimization. It can be applied in cases where it is necessary to find the minimum of a differentiable *objective function* $f(\boldsymbol{x})$ that is subject to a *constraint* $g(\boldsymbol{x})$, also represented by a differentiable function. In other words, we need to find the minima of the function f among the set of points $\boldsymbol{x}$ that satisfy the condition $g(\boldsymbol{x}) = 0$ [52]. All of the above can be expressed in a more compact form:

$$\begin{cases} \text{Minimize} \quad f\left(\boldsymbol{x}\right) = f\left(x_1, x_2, ..., x_n\right) \\ g\left(x_1, x_2, ..., x_n\right) = 0 \end{cases} \tag{3.19}$$

To satisfy both of the conditions listed in (3.19), the LM method requires to define a new objective function, called *Lagrangian* and defined as:

$$\mathcal{L}\left(\boldsymbol{x}, \lambda\right) = f\left(\boldsymbol{x}\right) + \lambda g\left(\boldsymbol{x}\right) \tag{3.20}$$

where the bold notation $\boldsymbol{x}$ is used to indicate a vector and will be adopted in the whole chapter. In equation (3.20), a new variable λ, called *Lagrange multiplier*, has been introduced. This variable has an arbitrary scalar value. Once the Lagrangian has been defined, the main and most important consequence of this technique is that the minima of the unconstrained objective function $\mathcal{L}$ are also minima of the original constrained problem [52]. Hence, by building the Lagrangian, one can turn a problem of constrained minimization into a simpler, unconstrained minimization, which is usually easier to solve. The method can also be generalized for a function that has to obey several constraints $g_i(\boldsymbol{x})$. In this case, $\mathcal{L}$ becomes:

$$\mathcal{L}\left(\boldsymbol{x}, \boldsymbol{\lambda}\right) = f\left(\boldsymbol{x}\right) + \sum_i \left(\lambda_i g_i\left(\boldsymbol{x}\right)\right) \tag{3.21}$$

which contains one Lagrange multiplier λ_i for each constraint g_i. From the mathematical point of view, the minimization of a function is connected with the fulfillment of two requirements, called first order condition (FOC) and second order condition (SOC) [53]. The FOC requires the gradient of the function to be null in the minimum point $(\boldsymbol{x}^*, \boldsymbol{\lambda}^*)$, while the SOC requires the Hessian matrix of the function to be positive definite. In the specific case of our function $\mathcal{L}$, the FOC can be written as:

$$\begin{cases} \nabla_\lambda \mathcal{L}\left(\boldsymbol{x}^*, \boldsymbol{\lambda}^*\right) = 0 \\ \nabla_x \mathcal{L}\left(\boldsymbol{x}^*, \boldsymbol{\lambda}^*\right) = 0 \end{cases} \tag{3.22}$$

where the Lagrangian is derived with respect to the Lagrange multipliers and the variables. The SOC instead is expressed as:

$$\vec{d}^T H_{\mathcal{L}}\left(\boldsymbol{x}^*, \boldsymbol{\lambda}^*\right) \vec{d} > 0 \quad \forall \vec{d} \tag{3.23}$$

$$\text{where } \left(H_{\mathcal{L}}\right)_{jk}\left(\boldsymbol{x}^*, \boldsymbol{\lambda}^*\right) = \frac{\partial^2 \mathcal{L}}{\partial x_j \partial x_k} \tag{3.24}$$

where $\vec{d}$ is any infinitesimal displacement from the minimum in the direction allowed by the constraints. Summing up, the minimization of $\mathcal{L}$ guarantees the minimization of $f\left(\boldsymbol{x}\right)$ within the constraints $g_i\left(\boldsymbol{x}\right)$, but also implies the fulfillment of conditions (3.22) and (3.23).

In some cases, equality constraints like the one in equation (3.19) can be too stringent, and it is useful to substitute them with inequality constraints:

$$k\left(\boldsymbol{x}\right) \leq 0 \tag{3.25}$$

However, the alteration of the constraints has to be accounted for in the Lagrangian: function $\mathcal{L}$ with the form described in equation (3.21) cannot be used anymore. It is therefore useful to introduce a new variable called *slack*, as explained in [54] and [55]. A slack variable is essentially used to convert the inequality into an equality. As a matter of fact, by adding a positive quantity to a negative number, we can make the number equal to zero.

$$k\left(\boldsymbol{x}\right) \leq 0 \tag{3.26}$$

$$k\left(\boldsymbol{x}\right) + t^2 = 0 \tag{3.27}$$

where t^2 is the slack variable, which is written in a quadratic form to denote that it must not be negative [54]. An analogous procedure can be adopted with inequalities of the opposite kind, i.e. containing a constraint of the “greater or equal” type. In that case, though, the slack variable has to be inserted with a negative sign. Therefore, in analogy with the previous case, by adding a negative quantity to a positive number, we can make the number equal to zero.

$$h\left(\boldsymbol{x}\right) \geq 0 \tag{3.28}$$

$$h\left(\boldsymbol{x}\right) - s^2 = 0 \tag{3.29}$$

Summing up, to be able to apply the LM method with inequality constraints it is necessary to introduce auxiliary variables, which are called slacks and must be squared to guarantee their positivity. According to the type of inequality, slacks will have a positive or negative sign to capture the inequality and turn it into an equality. Once this procedure has been adopted, it will also have an impact on the Lagrangian function, that must contain the new variables. The function $\mathcal{L}$ thus becomes:

$$\mathcal{L}\left(\boldsymbol{x}, \lambda_1, \lambda_2, t^2, s^2\right) = f\left(\boldsymbol{x}\right) + \lambda_1\left[k\left(\boldsymbol{x}\right) + t^2\right] + \lambda_2\left[h\left(\boldsymbol{x}\right) - s^2\right] \tag{3.30}$$

for a function f that has to obey constraints like the ones described in equations (3.26) and (3.28). Therefore, to find the minimum of $f\left(\boldsymbol{x}\right)$, equation (3.30) has to be minimized to find an optimal solution $(\boldsymbol{x}^*, \boldsymbol{\lambda}^*, t^{2*}, s^{2*})$. Once the minimization has been performed, based on the value of its Lagrange Multiplier λ, an inequality constraint can be defined *active* or *inactive*: the former has a non null multiplier and the corresponding slack variable is zero, while the latter has $\lambda = 0$ [55]. Therefore, in order to take into account the effects of the constraints we should expect them to be active.

3.3.1 LM Method implementation in the FOOT analysis code

The main goal of this thesis was to insert in the FOOT analysis code a procedure able to obtain from the A_1, A_2, A_3 values the best estimate of the number of mass A through the Lagrange Multipliers method. Since the LM method consists in defining an objective function $f(\boldsymbol{x})$ with some constraints $g_i(\boldsymbol{x})$ and building a Lagrangian function $\mathcal{L}$ that needs to be minimized (as described in section 3.3), I should include the parameter A in a Lagrangian function. More precisely, it has to be included in vector $\boldsymbol{x}$, from which the Lagrangian depends, so that the best estimate is obtained by taking the value of A in the point $\boldsymbol{x}^*$ which minimizes $\mathcal{L}$. The best estimate of A will, from now on, be referred to as A_{fit}. In this section, all the necessary steps for the computation of A_{fit} will be described.

- *Definition of the objective function f($\boldsymbol{x}$)*
  For the analysis work of this thesis, I chose to include the parameter A in the objective function, i.e. the function that needs to be minimized

and needs to fulfill the constraints. Including A in the objective function is not enough: it must be at least in a quadratic form, in order to have non null first and second derivatives and satisfy conditions (3.22) and (3.23).
Taking all of the above considerations into account, the function I inserted in the procedure is:

$$f(\boldsymbol{x}) = (A_1 - A_{fit})^2 + (A_2 - A_{fit})^2 + (A_3 - A_{fit})^2 \tag{3.31}$$

i.e., the sum of the squared differences between the three correlated values of A and the value of the best estimate. It is important to retrieve equations (3.8), (3.12) and (3.17), which contain the dependence of the variables A$_1$, A$_2$ and A$_3$ on the kinematic quantities of the fragments. Equation (3.31) can thus be written as:

$$f(\boldsymbol{x}) = \left(\frac{p}{U\beta\gamma} - A_{fit}\right)^2 + \left(\frac{E_k}{U(\gamma-1)} - A_{fit}\right)^2 + \left(\frac{p^2 - E_k^2}{2UE_k} - A_{fit}\right)^2 \tag{3.32}$$

where the convention $c = 1$ has been adopted. It is also worth to remind the reader that γ is equivalent to:

$$\gamma = \frac{1}{\sqrt{1-\beta^2}} = \frac{1}{\sqrt{1 - \frac{L^2}{TOF^2 \cdot c^2}}} \tag{3.33}$$

where L is the trajectory of the fragment inside the detector (i.e., from its production point to the calorimeter). Equations (3.32) and (3.33) show that the vector of variables from which our problem will depend contains the three kinematic quantities of the fragment and the best estimate of A, therefore:

$$f(\boldsymbol{x}) = f(p, TOF, E_k, A_{fit}) \tag{3.34}$$

- *Definition of constraints $g_i(\boldsymbol{x})$*
  In the specific case of this analysis, an equality constraint like the one in (3.19) is not advantageous or useful to obtain information about the best estimate A_{fit}. It is easier and more practical to impose for the objective function (3.32) some inequality constraints. The ones I chose to apply are three and involve the momentum, the time of flight and

the kinetic energy of fragments:

$$\left(\frac{p_{meas}-p}{\sigma_P}\right)^2 \leq 1 \tag{3.35}$$

$$\left(\frac{TOF_{meas}-TOF}{\sigma_{TOF}}\right)^2 \leq 1 \tag{3.36}$$

$$\left(\frac{E_{kmeas}-E_k}{\sigma_{E_k}}\right)^2 \leq 1 \tag{3.37}$$

where p_{meas}, TOF_{meas}, E_{kmeas} indicate the MC-generated momentum, time of flight and kinetic energy after a gaussian smearing, in order to reproduce the measured quantities. The conditions (3.35), (3.36), (3.37) require that, for a given track, the fitted momentum, time of flight and kinetic energy, i.e. the elements in the vector $\boldsymbol{x}$ from which the Lagrangian depends, are within one standard deviation from the corresponding measured quantity of the same track (i.e., p_{meas}, TOF_{meas}, $\mathrm{E}_{k_{meas}}$). Constraints (3.35), (3.36) and (3.37) are inequalities of the “smaller or equal” type: therefore, to build the Lagrangian we must introduce a slack with positive sign, using the procedure described in equation (3.27). In this way, the constraints become:

$$\left(\frac{p_{meas}-p}{\sigma_P}\right)^2 - 1 + s_1^2 = 0 \tag{3.38}$$

$$\left(\frac{TOF_{meas}-TOF}{\sigma_{TOF}}\right)^2 - 1 + s_2^2 = 0 \tag{3.39}$$

$$\left(\frac{E_{kmeas}-E_k}{\sigma_{E_{kin}}}\right)^2 - 1 + s_3^2 = 0 \tag{3.40}$$

- *Definition and minimization of the Lagrangian $\mathcal{L}$*
  Once all the basic elements for the construction of the Lagrangian have been defined, it is necessary to retrieve equation (3.30). By inserting the function (3.32) and the constraints (3.38), (3.39) and (3.40) in it, we obtain:

$$\begin{aligned}\mathcal{L}\left(\boldsymbol{x},\boldsymbol{\lambda},\boldsymbol{s^2}\right) &= \left(\frac{p}{U\beta\gamma} - A_{fit}\right)^2 + \left(\frac{E_k}{U\left(\gamma-1\right)} - A_{fit}\right)^2 + \left(\frac{p^2-E_k^2}{2UE_k} - A_{fit}\right)^2 \\ &+ \lambda_1\left[\left(\frac{p_{meas}-p}{\sigma_P}\right)^2 - 1 + s_1^2\right] + \lambda_2\left[\left(\frac{TOF_{meas}-TOF}{\sigma_{TOF}}\right)^2 - 1 + s_2^2\right] \\ &+ \lambda_3\left[\left(\frac{E_{kmeas}-E_k}{\sigma_{E_{kin}}}\right)^2 - 1 + s_3^2\right]\end{aligned} \tag{3.41}$$

which is the function to minimize to obtain A_{fit}. On the right side of the equation, a compact notation has been used to indicate the vectors of variables $\boldsymbol{x}$, Lagrange multipliers $\boldsymbol{\lambda}$ and slacks $\boldsymbol{s_i^2}$:

$$\boldsymbol{x} = (p, TOF, E_k, A_{fit}) \tag{3.42}$$

$$\boldsymbol{\lambda} = (\lambda_1, \lambda_2, \lambda_3) \tag{3.43}$$

$$\boldsymbol{s_i^2} = \left(s_1^2, s_2^2, s_3^2\right) \tag{3.44}$$

The minimization of the Lagrangian (3.41) has been commissioned to the MINUIT algorithm of the ROOT package [56]. MINUIT works with a user defined function and performs the minimization in an iterative way: at each step, the value of the function is computed and the values of the free parameters on which it depends are varied, in order to understand in which direction the algorithm has to perform the subsequent parameters variation to reach the minimum point. The maximum number and size of steps can be defined by the user, together with the range in which the parameters can take values. Once the algorithm has reached the minimum of the function, it provides the values of parameters producing such minimum, together with their error matrix. In this specific case, $\mathcal{L}$ has been inserted in the code and the components of vectors $\boldsymbol{x}, \boldsymbol{\lambda}, \boldsymbol{s_i^2}$ have been treated as free parameters with limits. The minimization of the Lagrangian thus produced some values that we can indicate as $\boldsymbol{x}^*, \boldsymbol{\lambda}^*, \boldsymbol{s_i^2}^*$, from which A_{fit} has been extracted and studied for each track. Together with free parameters, MINUIT allows the definition of fixed parameters: in this analysis, p_{meas}, TOF_{meas}, $E_{k_{meas}}$ have been considered fixed and set to the output value of the MC simulation with the corresponding Gaussian smearing.

3.4 Analysis Results with LM Method

As mentioned above, the main goal of the analysis consist in finding the optimal values $\boldsymbol{x}^*, \boldsymbol{\lambda}^*$ and $\boldsymbol{s_i^2}^*$, able to minimize the Lagrangian function (3.41). Among all of these values, the most important one for my thesis is the mass number A_{fit}, which represents the best estimate of A for nuclear fragments. This value includes the information from the three redundant measurements A_1, A_2 and A_3 provided by the FOOT detector, in this case obtained from simulated MC data and smeared of a percentage related to the experimental resolutions of detectors, in order to get a real data-like sample. The analysis code receives quantities in vectors (3.42), (3.43) and (3.44) as free parameters, meaning that the MINUIT algorithm can change their values in the optimal way to reach the minimum of $\mathcal{L}$, ranging in an interval that can be set by the user. For the kinematic quantities of fragments, i.e. the momentum, time of flight and kinetic energy, the MC output value can be used as a starting value, and also their optimal range can be extrapolated from simulations. Moreover, it is known from the theory exposed in section 3.3 that slacks must be positive quantities, in our case at most equal to 1. For Lagrange Multipliers, instead, it is more difficult to have a reliable prediction: before performing the LM fit procedure, a performance study is necessary to understand what are the best ranges and starting values for $\boldsymbol{\lambda}$.

3.4.1 Performance study of Lagrange Multipliers

The first thing that needs to be evaluated is the sign of quantities contained in vector (3.43), i.e. understand if they have to be positive, negative or both.

Setting negative values for lambdas in the range [-1;0], the minimization procedure is not able to converge, and the reconstructed distribution of A_{fit} does not have a definite value for any of the analysed fragments. The same happens when a still lower boundary is set for the range: this hints at positive values for the Lagrange multipliers. As a matter of fact, when a positive range is set for λ_1, λ_2, λ_3, the minimization has a successful outcome for all fragments. The fit result depends on the upper boundary of the range and on the starting value set for the multipliers. Fitting the reconstructed A_{fit} distributions with a Gaussian function, the mean value increases when a larger range is set for the variables, and so does the percentage resolution. The starting value does not affect the output of the minimization too much: it is only slightly worse in the case in which the starting value is set to half of the maximum. All of the above considerations are summed up in figures 3.12(a) and 3.12(b) for ^{12}C, but they are valid for all the studied fragments. The studied ranges are: [0;0.3], [0;1], [0;5], [0;10] and [0;20]. The performance study proved that the method exhibits a systematic effect, causing the results of the fit to improve as the range of Lagrange multipliers gets narrower: the reason for this behavior is still under investigation. In the present analysis the range [0;1] has been chosen, in order to have a trade-off between the performances and the choice of a range narrow enough to weigh the constraints in the proper way.

Once we have found out that vector $\boldsymbol{\lambda}$ must contain positive values and once we have chosen the optimal range and starting values for the multipliers, the fit procedure has been carried out. Its results will be described in next section.

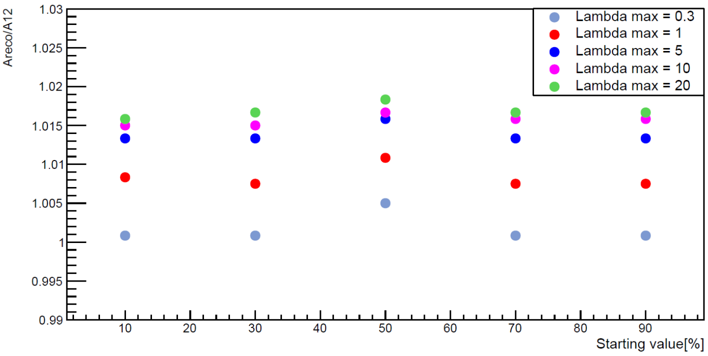

(a) Reconstructed/Expected Mass Number

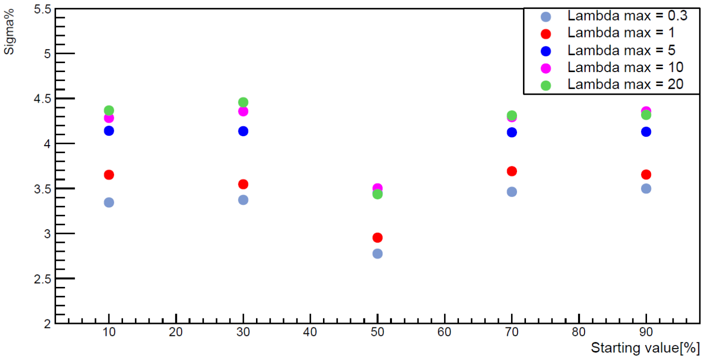

(b) Percentage Resolution

Figure 3.12: Performance study for the range and starting values of Lagrange multipliers, based on the outcome of reconstructed mass number and resolution for ^{12}C. In both plots, on the x axis are reported the starting values of Lagrange Multipliers expressed as percentages of the maximum value of lambda reported in the legend panel (i.e., Lambda max). On the y axis, in (a) A_{reco} indicates the value obtained from a Gaussian fit of the reconstructed peak and A_{12} is the expected value (i.e., 12); in (b) $\sigma_{\%}$ is obtained from the Gaussian fit of the number of mass peak and expressed as a percentage of the mean value.

Variable	Starting Value	Boundlow	Boundup
p	p_{MC}	0	30 GeV/c^2
TOF	TOF_{MC}	0	30 ns
E_k	E_{kMC}	0	15 GeV
A	$2Z_{reco}$	0	20
λ_1	0.3	0	1
λ_2	0.3	0	1
λ_3	0.3	0	1
s_1	not set	-1	1
s_2	not set	-1	1
s_3	not set	-1	1

Table 3.3: Starting values and ranges of free parameters used in the minimization of the Lagrangian for the reconstruction of the best estimate for the mass number.

3.4.2 Isotopic Identification with LM method

In this section, the distributions of A_{fit}, i.e. the best estimate of the mass number of fragments, obtained by the minimization of function (3.41), are reported. Differently from all the previously reported results, this analysis has only been performed for a beam of 200 MeV/u hitting a polyethylene target. The reason why the 700 MeV/u beam has not been taken into account is that the LM method calculation involves A_1, A_2 and A_3, but only A_1 is used for the evaluation of A for fragments produced by a 700 MeV/u beam. This is because A_2 and A_3 contain the kinetic energy, which at higher energies is largely underestimated due to the abundant neutron production in the calorimeter, as described in section 3.2.
Since the kinematic variables, Lagrange multipliers and slacks have been inserted in the MINUIT algorithm as free parameters with limits, table 3.3 reports the ranges and starting values assigned to such parameters to obtain the presented results. All values in the table have either been obtained by comparison with simulations or by theoretical considerations exposed in the previous sections.

It is important to underline that negative values were allowed for the slacks s_1,s_2,s_3 because they appear in the Lagrangian in a quadratic form.
Besides the correctly reconstructed number of mass of fragments, a further proof of the good functioning of the method can be found in the distributions of Lagrange multipliers and slacks, reported in figure 3.13 for ^{12}C. As a matter of fact, the distributions show that λs are mostly non null and that slacks have a peak at 0. Moreover, by applying a χ^2 cut as described in the following

Fragment	A_1	$\sigma\,(A_1)\,\%$	A_2	$\sigma\,(A_2)\,\%$	A_3	$\sigma\,(A_3)\,\%$	A_{LM}	$\sigma\,(A_{LM})\,\%$
^{7}Li	7.05	4.2	6.97	4.0	7.18	9.0	7.04	4.0
^{9}Be	9.07	4.3	8.95	3.8	9.25	9.0	9.04	3.9
^{11}B	11.10	4.2	10.93	3.7	11.34	8.9	11.06	3.7
^{12}C	12.16	4.1	11.90	3.3	12.49	8.8	12.09	3.5
^{14}N	14.25	4.1	13.90	3.3	14.71	9.0	14.12	3.4
^{16}O	16.31	4.0	15.87	3.3	16.89	8.9	16.13	3.2

Table 3.4: Comparison among the values of A obtained with formulas (3.8), (3.12), (3.17) and values obtained with the LM fit.

it is possible to discard the badly reconstructed events corresponding to null λs and non null slacks, thus confirming the requirement of active constraints explained in section 3.3. It is also worth to notice that, even if the values assumed by lambdas are close to the upper and lower boundary of the range, this does not cause any problem in the reconstruction outcome.

By fitting the A_{fit} distributions produced by the minimization of $\mathcal{L}$ with a Gaussian function, I obtained the mean values and resolutions for the best estimate of the mass number. The results of the fit procedure show an improvement in mean values and resolutions with respect to the values of A_1, A_2, A_3, as summed up in table 3.4 for the most abundant fragments of each charge. Besides improving the A values, the procedure is also able to keep the percentage resolution of A_{fit} below 4% for such fragments. The performance improvement is not that great (for example with respect to A_2) because the precision of TOF and E_k is larger than the one of the momentum, thus using all the quantities at the same time does not cause big changes.

Some small tails, though, are still visible in the plots, next to the fitted peaks. A further improvement can thus be applied to the data, by identifying these badly reconstructed events using their χ^2 value. Figure 3.14 shows the distribution of χ^2 as a function of A_{fit} for some of the most abundant fragments produced in the reaction: from the plots it is evident that a χ^2 cut at 5 can help eliminating the undesired event without reducing the statistics too much (i.e. with a reduction that is less than 10% of the events) and it is compatible with the results in statistic proposed by the methods in [50, 51]. The improvement can be seen for the most abundant fragment of each charge in figures 3.15 and 3.16, where plots on the left show all the reconstructed events for each fragment, while plots on the right show the distributions after a χ^2 cut: the cut is able to discard all the events in the tails.

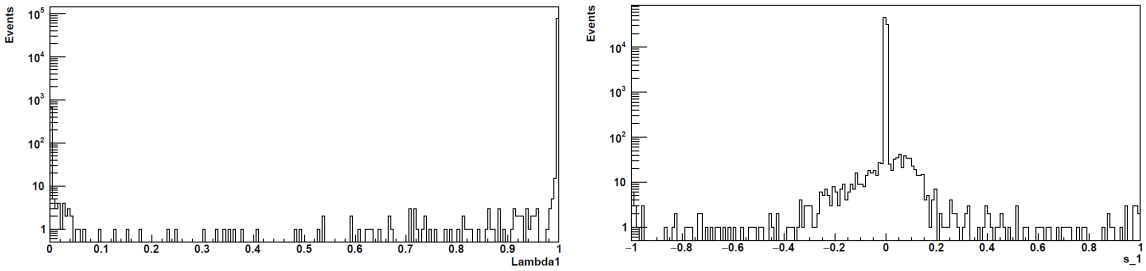

(a) λ_1 distribution (b) s_1 distribution

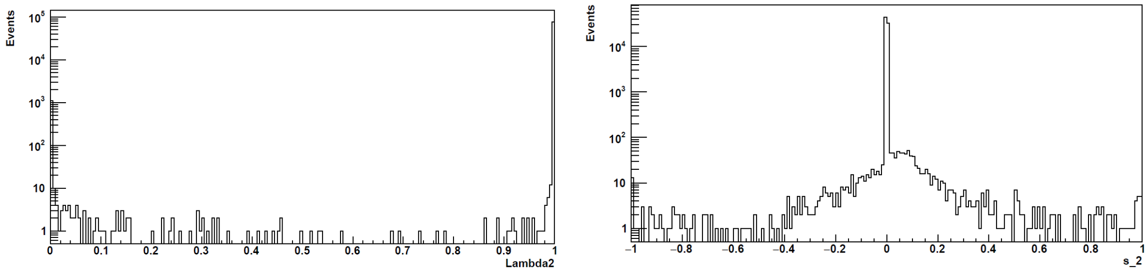

(c) λ_2 distribution (d) s_2 distribution

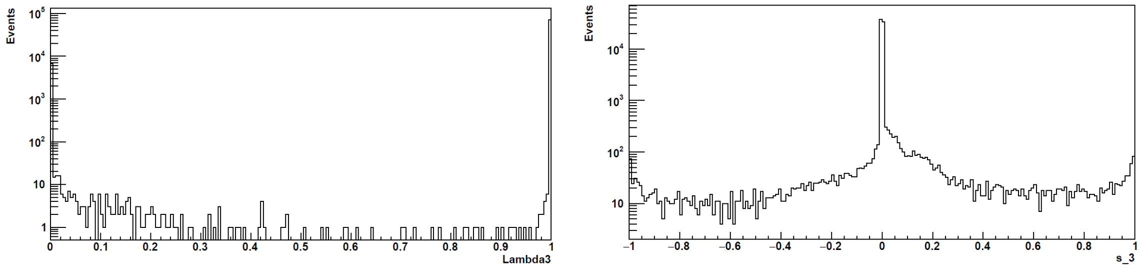

(e) λ_3 distribution (f) s_3 distribution

Figure 3.13: Distribution of Lagrange multipliers and slacks obtained by the minimization of the Lagrangian function (3.41). All distributions show that the three constraints applied to the function are active.

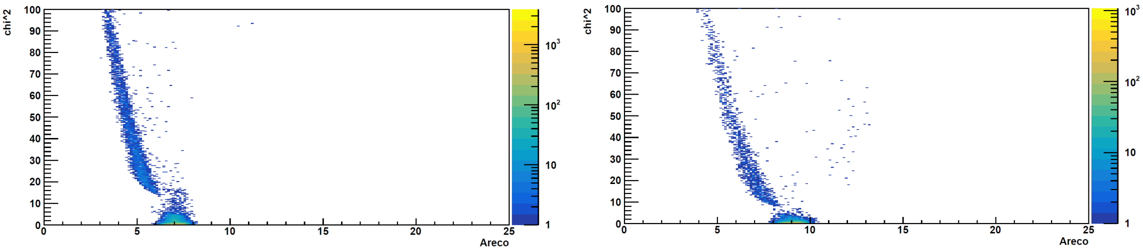

(a) ^{7}Li (b) ^{9}Be

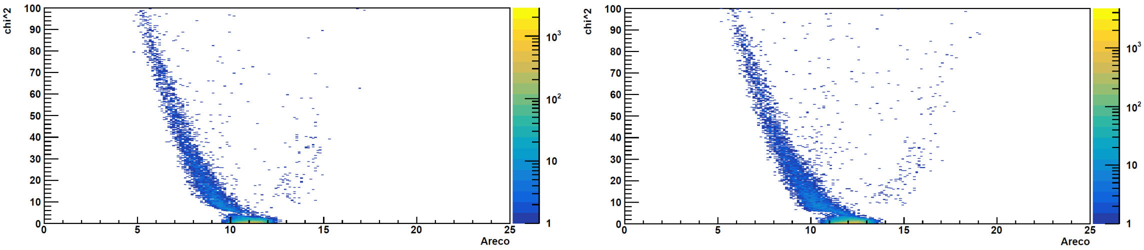

(c) ^{11}B (d) ^{12}C

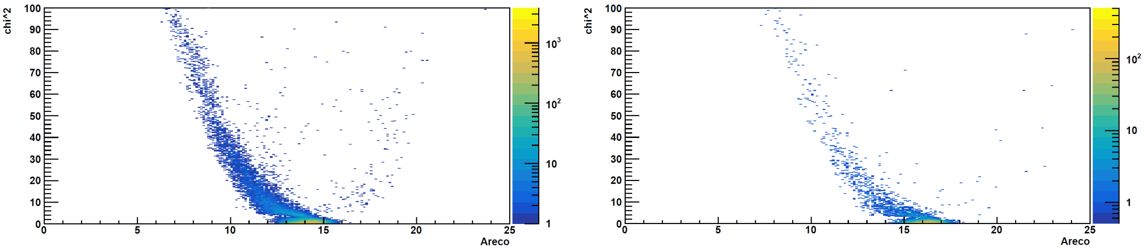

(e) ^{14}N (f) ^{16}O

Figure 3.14: Distribution of χ^2 values as a function of A_{fit}: a cut at a value of 5 (yellow area in plots) allows to eliminate badly-reconstructed events in the tail, without ruining the reconstruction statistics.

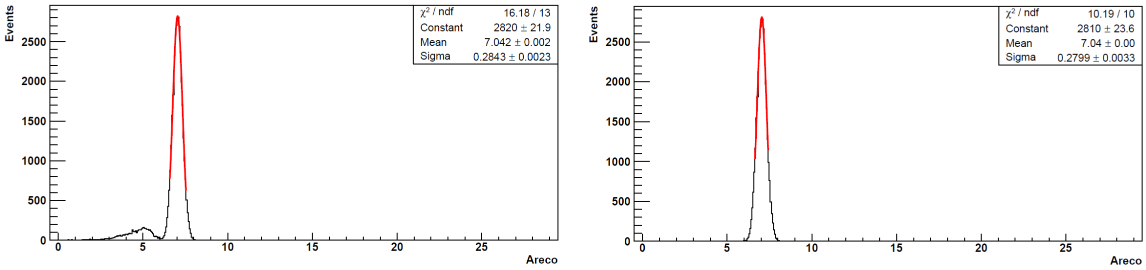

(a) ^{7}Li (b) ^{7}Li with $\chi^2 < 5$

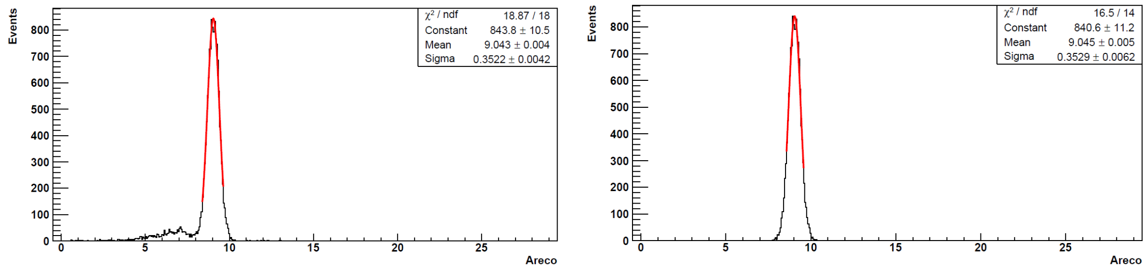

(c) ^{9}Be (d) ^{9}Be with $\chi^2 < 5$

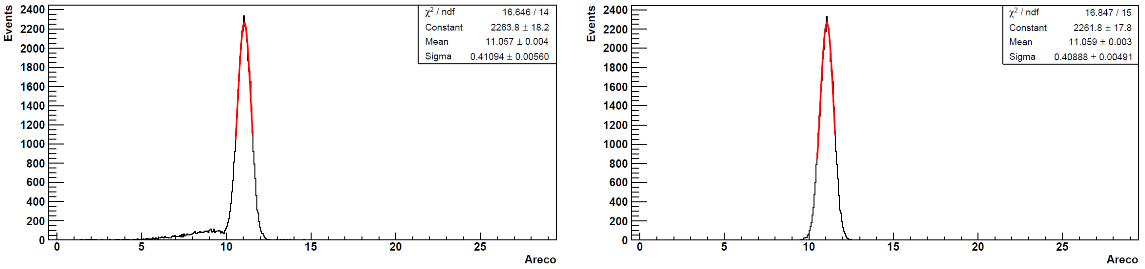

(e) ^{11}B (f) ^{11}B with $\chi^2 < 5$

Figure 3.15: Reconstructed Li, Be, B fragments using the LM method. Plots are shown without any event selection (on the left) and with a χ^2 cut to eliminate tails of badly-reconstructed events (on the right).

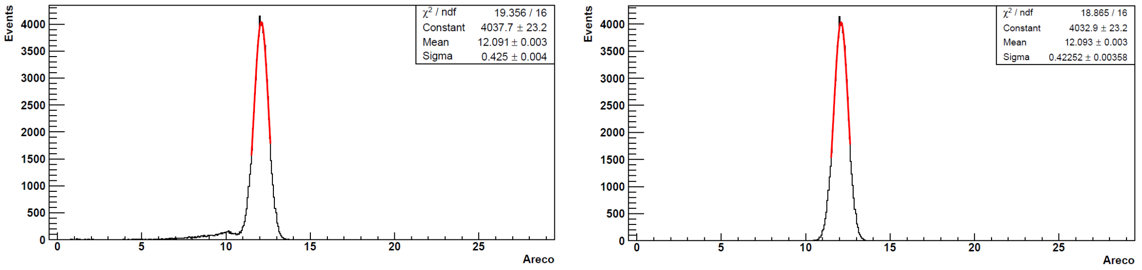

(a) ^{12}C

(b) ^{12}C with $\chi^2 < 5$

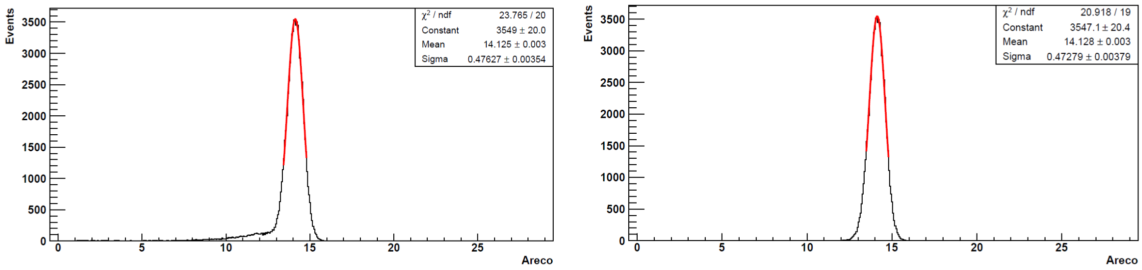

(c) ^{14}N

(d) ^{14}N with $\chi^2 < 5$

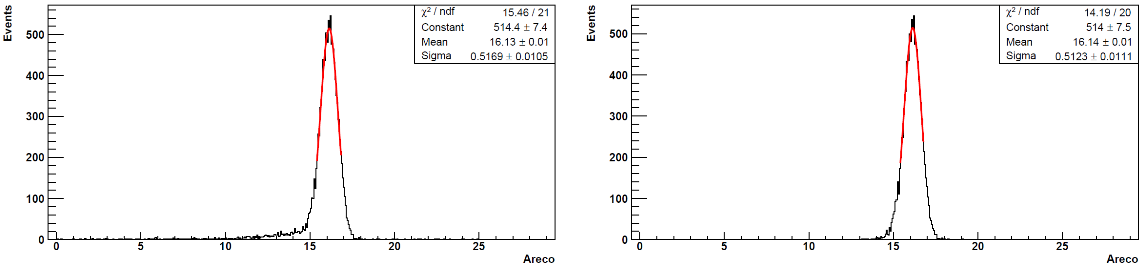

(e) ^{16}O

(f) ^{16}O with $\chi^2 < 5$

Figure 3.16: Reconstructed C, N, O fragments using the LM method. Plots are shown without any event selection (on the left) and with a χ^2 cut to eliminate tails of badly-reconstructed events (on the right).

Fragment	A^{cut}_{LM}	$\sigma\left(A^{cut}_{LM}\right)\%$	A^{cut}_{ALM}	$\sigma\left(A^{cut}_{ALM}\right)\%$	$A^{cut}_{\chi^2}$	$\sigma\left(A^{cut}_{\chi^2}\right)\%$
^{6}Li	6.05	4.1	6.01	3.9	6.08	4.2
^{7}Li	7.04	4.1	7.02	3.8	7.09	4.2
^{8}Li	8.04	4.1	8.05	4.2	8.10	4.2
^{7}Be	7.07	4.0	7.01	3.4	7.12	4.2
^{9}Be	9.04	3.9	9.00	3.6	9.12	4.2
^{10}B	10.08	3.7	9.99	3.6	10.16	4.1
^{11}B	11.06	3.7	11.00	3.4	11.16	4.1
^{12}B	12.05	3.7	12.04	4.6	12.17	4.1
^{9}C	9.13	3.1	9.0	4.9	9.28	4.2
^{10}C	10.14	3.8	10.02	3.3	10.23	4.2
^{11}C	11.13	3.6	11.00	3.3	11.23	4.1
^{12}C	12.09	3.5	11.96	3.2	12.22	4.1
^{13}C	13.07	3.5	12.96	3.3	13.22	4.1
^{14}C	14.06	3.5	13.98	3.4	14.23	4.1
^{12}N	12.05	3.9	12.05	5.0	12.21	4.3
^{13}N	13.14	3.5	12.98	3.1	13.32	4.1
^{14}N	14.13	3.4	13.97	3.3	14.26	4.1
^{15}N	15.08	3.4	14.95	3.3	15.29	4.1
^{14}O	14.07	3.6	13.96	3.0	14.37	4.2
^{15}O	15.16	3.4	14.96	3.1	15.35	4.1

Table 3.5: Comparison between mean values and resolutions obtained by a Gaussian fit of A fit results for three different procedures: Lagrange Multipliers, χ^2, ALM. Fragments are produced by a 200 MeV/u ^{16}O beam on a polyethylene target.

Finally, the results of my analysis can be compared to the ones obtained with the χ^2 minimization [50] and the ALM [51], i.e. other fit procedures already implemented in the FOOT analysis code. All results are reported in table 3.5 for a wide variety of fragments, where values that are not related to the LM method have been taken from [50] and [51]. From the table it emerges that, extending the LM method to other fragments, the worse reachable resolution is 4.1%. The results of the three techniques are summed up in figure 3.17. The figure shows that the LM method provides results that are compatible with the ones obtained with χ^2 minimization and ALM, in both mean values and resolutions of fitted Gaussian peaks.

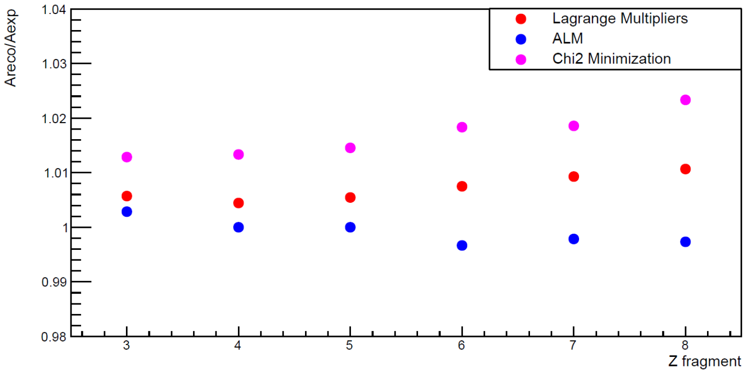

(a) Reconstructed/Expected Mass Number

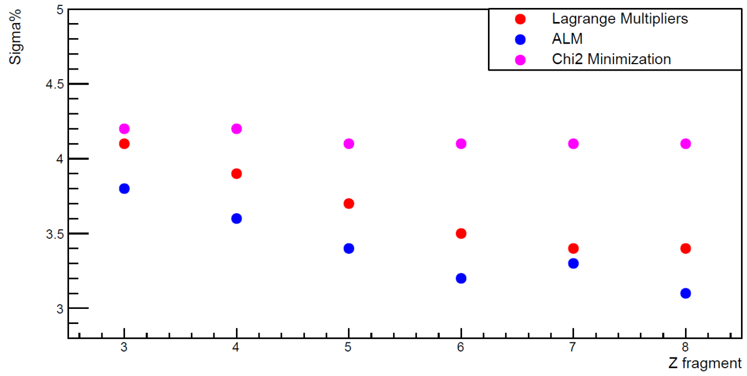

(b) Percentage Resolution

Figure 3.17: Comparison between the mean values (a) and percentage resolutions (b) of the three mass reconstruction methods. The reported values are obtained from the fit of reconstructed peaks with a Gaussian distribution, for the most abundant fragments of each charge.

Conclusions

The main goal of this work is to implement a procedure based on the Lagrange multipliers (LM) method for the number of mass A reconstruction in the analysis code of the FOOT (FragmentatiOn Of Target) experiment. The aim of the procedure is to obtain the best estimate of the number of mass A of fragments from the three redundant measurements A_1, A_2, A_3 acquired by the apparatus. Together with the charge Z, the number of mass A_{fit} obtained by the LM fit will allow to uniquely identify the fragments produced in the beam-target interactions. The method of this reconstruction procedure will then be used to compute the target fragmentation cross section, using an inverse kinematic approach, and the projectile one. Moreover, the results can provide information about hadrontherapy and space radioprotection. In the present work, fragments have been reconstructed using Monte Carlo (MC) simulated data, obtained by a FLUKA simulation of the electronic setup of the apparatus which is specifically built for the detection of heavy ($Z>2$) fragments. The data analysed in the present work represent the fragmentation of a ^{16}O beam with two different energies of the primary beam: 200 MeV/u, compatible with the hadrontherapy energy range, and 700 MeV/u, compatible with data needed for space radioprotection, on a C_2H_4 target. In both cases, a smearing corresponding to the resolution of subdetectors has been applied to simulated data: this allowed to obtain a real data like sample. The quantities involved in the Z reconstruction are the energy loss of the particle in a thin scintillator and the time of flight. For the A reconstruction, time of flight (TOF), momentum (p) and kinetic energy (E_k) are used. For the reconstructed Z, both 200 and 700 MeV/u beam energies allowed a good charge separation, with a resolution that ranges from $\sim 3\%$ for heavy fragments to $\sim 6\%$ for hydrogen. The inefficiencies in the reconstruction of light fragments (i.e., Z=1,2) , though, will be compensated by data obtained with the emulsions setup. After the charge identification, the number of mass of the produced fragment has been computed in three different ways by combining respectively TOF and p, TOF and E_k and p and E_k. The three obtained correlated values for the most abundant fragment of each charge are compatible with the expected A. The largest shifts with respect to the true A value are observed in A_2 and A_3: as a matter of fact, these two involve the kinetic energy of fragments, which suffers from an underestimation caused by the large neutron production in the calorimeter. This phenomenon is amplified at 700 MeV/u: therefore, in this case only A_1 is used for the number of mass reconstruction. Being the three A measurements correlated, i.e. with a subdetector in common for each couple of measurements, one needs to combine them with a fit procedure to obtain a best estimate A_{fit}. This is precisely what the LM method has been used for, using data related to the 200 MeV/u beam. Lagrange multipliers are normally used for constrained minimization of functions: A_{fit} thus needs to be inserted in the vector of parameters from which the Lagrangian function depends. Then, its best estimate will be obtained as the value of the parameter in the minimum of the Lagrangian $\mathcal{L}$. With $\mathcal{L}$ described in Chapter 3, the minimization can be performed and A can be correctly reconstructed. The parameters inserted in the function are: A_1, A_2, A_3 and A_{fit}, together with the kinematic quantities TOF, p, E_k. Moreover, lagrange multipliers λ_i and slacks s_i^2 were introduced: these are both characteristics of the LM method. It is important to underline that, for the correct functioning of the algorithm, λ must be positive quantities. In this work, a preliminary study of their ranges and starting values has been performed: the best range was proven to be [0;1], independently from their starting value. The correct output of the LM fit can be improved by performing a χ^2 cut at a value of 5 on A_{fit}. For all the investigated fragments, the percentage resolution of A is within 4%. Moreover, a comparison with the other fit methods already implemented in the FOOT reconstruction, i.e. χ^2 minimization and Augmented Lagrangian Method (ALM), proved that the statistics and results are compatible: for some fragments, the LM method can also provide some improvements, mostly in the expected values A_{fit}. In conclusion, the study proposed in the present thesis work provides encouraging results to be employed as starting points for further investigations and analyses based on the Lagrange Multipliers method and aimed at optimizing the number of mass reconstruction.

Bibliography

[1] `https://www.who.int/news-room/fact-sheets/detail/cancer`

[2] G. Battistoni et al. (FOOT collaboration) *Measuring the Impact of Nuclear Interaction in Particle Therapy and in Radio Protection in Space: the FOOT Experiment.* Frontiers in Physics 8, 2021.

[3] R. Nuraini and R. Widita. *Tumor Control Probability (TCP) and Normal Tissue Complication Probability (NTCP) with Consideration of Cell Biological Effect.* J. Phys.: Conf. Ser. 1245 012092, 2019.

[4] Chang D.S., Lasley F.D., Das I.J., Mendonca M.S., Dynlacht J.R. *Therapeutic Ratio. In: Basic Radiotherapy Physics and Biology.* Springer, 2014.

[5] W. R. Leo. *Techniques for Nuclear and Particle Physics Experiments.* Springer, 1994.

[6] D. Schardt, T. Elsässer, D. Schulz-Ertner. *Heavy-ion tumor therapy: physical and radiobiological benefits.* Rev. Mod. Phys. 82, 383, 2010.

[7] D. R. Grimes, D.R. Warren, M. Partridge. *An approximate analytical solution of the Bethe equation for charged particles in the radiotherapeutic energy range.* Sci Rep 7, 9781, 2017.

[8] S. Bijan Jia et al. *Designing a range modulator wheel to spread-out the Bragg peak for a passive proton therapy facility.* Nuclear Instruments and Methods in Physics Research A 806, 2016.

[9] `https://www.britannica.com/science/range-particle-radiation`

[10] H.P Schietz *Key Nuclear Reaction Experiments- Chapter 2: Rutherford scattering and the atomic nucleus.* IOP Publishing, 2015.

[11] H.A.Bethe *Moliere's theory of Multiple Scattering.* Phys. Rev. 89, 6, 1953.

[12] M. Durante and H. Paganetti. *Nuclear physics in particle therapy: a review.* Rep. Prog. Phys. 79 096702, 2016.

[13] J. Bowman, W. Swiatecki, C. Tsang. *Abrasion and Ablation of Heavy Ions.* Lawrence Berkeley National Laboratory, 1973.

[14] F. Tommasino, M. Durante *Proton Radiobiology.* Cancers 7(1):353-381, 2015.

[15] E. Haettner, H. Iwase, D. Schardt. *Experimental fragmentation studies with ^{12}C therapy beams.* Radiat Prot Dosimetry ;122(1-4):485-7, 2006.

[16] E.B. Podgorsak. *Radiation Oncology Physics: a handbook for teachers and students.* International Atomic Energy Agency, 2005.

[17] J. Loeffler M. Durante. *Charged particle therapy — optimization, challenges and future directions.* Nat. Rev. Clin. Oncol. 10, 2013.

[18] U. Amaldi. *History of Hadrontherapy.* Modern Physics Letters A 30 (17), 2015.

[19] Particle Therapy Co-operative Group website: `https://www.ptcog.ch/`

[20] J.W. Norbury et al. *Review of Nuclear Physics Experiments for Space Radiation.*, 2011.

[21] J. Wilson et al. *Galactic and solar cosmic ray shielding in deep space.* NASA Technical Paper NASA TP-3682, 1997.

[22] J.W. Wilson et al. *Shielding Strategies for Human Space Exploration.* NASA Conference Publication 3360, 1997.

[23] C. Zeitlin, C. La Tessa *The Role of Nuclear Fragmentation in Particle Therapy and Space Radiation Protection.* Frontiers in Oncology 6, 2016.

[24] M. De Napoli et al. *Carbon fragmentation measurements and validation of the GEANT4 nuclear reaction models for hadrontherapy.* Phys. Med. Biol. 57, 2012.

[25] J. Dudouet et al. *Zero-degree measurements of ^{12}C fragmentation at 95 MeV/nucleon on thin targets.* Phys. Rev. C 89:064615, 2014.

[26] M. Toppi et al. *Measurement of fragmentation cross sections of 12C ions on a thin gold target with the FIRST apparatus.* Phys. Rev. C 93:064601, 2016.

[27] J. Dodouet et al. *Double-differential fragmentation cross-section measurements of 95 MeV/nucleon* ^{12}C *beams on thin targets for hadron therapy.* Phys. Rev. C 88(2), 2013.

[28] T.T. Böhlen et al. *The FLUKA Code: Developments and Challenges for High Energy and Medical Applications.* Nuclear Data Sheets 120, 2014.

[29] A. Ferrari et al. *FLUKA: A multi-particle transport code.* CERN-2005-010, SLAC-R-773, INFN-TC-05-11, CERN-2005-10, 2005.

[30] S.M. Valle, A. Alexandrov et al. *FOOT: a new experiment to measure nuclear fragmentation at intermediate energies.* Perspectives in Science 12, 2019.

[31] L. Galli et al. *WaveDAQ: An highly integrated trigger and data acquisition system.* Nucl. Instrum Meth. A 936, 2019.

[32] Z. Abou-Haidar et al. *Performance of upstream interaction region detectors for the FIRST experiment at GSI.* JINST 7, 2012.

[33] D. Yunsheng et al. *The Drift Chamber detector of the FOOT experiment: performance analysis and external calibration.* Nuclear Instruments and Methods in Physics Research A 986, 2021.

[34] N. Simos et al. *Demagnetization of* Nd_2Fe_14B, $Pr_2Fe_{14}B$ *and* Sm_2Co_{17} *permanent magnets in spallation irradiation fields.* IEEE T. Magn. 54, 2018.

[35] W. de Boer et al. *Measurements with a CMOS pixel sensor in magnetic fields.* Nuclear Instruments and Methods in Physics Research A 487, 2002.

[36] PLUME website: `www.iphc.cnrs.fr/PLUME.html`

[37] S. Meroli et al. *Energy loss measurement for charged particles in very thin silicon layers.* JINST 6, 2011.

[38] O. Adriani et al. *Comprehensive study of the effects of irradiation on charge collection efficiency in silicon detectors.* Nucl. Instr. Meth A 396, 1997.

[39] B. Alpat et al. *The internal alignment and position resolution of the AMS-02 silicon tracker determined with cosmic-ray muons.* Nucl. Instr. Meth. A 613, 2010.

[40] L. Scavarda *Design and performance of the Calorimeter for the FOOT experiment.* Il nuovo cimento C 4, 2020.

[41] G. De Lellis et al. *Emulsion Cloud Chamber technique to measure the fragmentation of a high-energy carbon beam.* JINST 2, 2007.

[42] G. De Lellis et al. *Measurements of the fragmentation of Carbon nuclei used in hadron therapy.* Nuclear Physics A 853, 2011.

[43] M.C. Montesi et al. *Ion charge separation with new generation of nuclear emulsion films.* De Gruyter - Open Physics 17, 2019.

[44] N.Agafonova et al. *Momentum measurements by the multiple coulomb scattering method in the OPERA lead-emulsion target.* New J. Phys. 14, 2012.

[45] M. De Serio et al. *Momentum measurement by the angular method in the Emulsion Cloud Chamber.* Nucl. Instr. Meth. A 512(3), 2003.

[46] G. Battistoni et al. *The FLUKA Code: An Accurate Simulation Tool for Particle Therapy.* Frontiers in Oncology 6, 2016.

[47] V.Vlachoudis. *FLAIR: A Powerful But User Friendly Graphical Interface For FLUKA.* Proc. Int. Conf. on Mathematics, Computational Methods Reactor Physics, 2009.

[48] G.Traini et al. *Performance of the ToF detectors in the FOOT experiment.* Il nuovo cimento 43, 2020.

[49] J. Rauch T.Schlüter *GENFIT - a Generic Track-Fitting Toolkit.* J. of Phys. Conf. Series 608, 2015.

[50] S. Colombi. *Nuclear fragmentation in particle therapy and space radiation protection: from the standard approach to the FOOT experiment.* PhD Thesis, 2021.

[51] S. M. Valle. *Design, simulation and performances study of the FOOT experiment.* PhD thesis, 2019.

[52] `http://www.cs.toronto.edu/~mbrubake/teaching/C11/Handouts/LagrangeMultipliers.pdf`

[53] W.S. Cho et al. *OPTIMASS: A Package for the Minimization of Kinematic Mass Functions with Constraints.* Journal of High Energy Physics 26, 2016.

[54] `https://users.wpi.edu/~pwdavis/Courses/MA1024B10/1024_Lagrange_multipliers.pdf`

[55] `https://machinelearningmastery.com/lagrange-multiplier-approach-with-inequality-constraints/`

[56] `https://root.cern.ch/download/minuit.pdf`